# Identifying the *meta*, *para* and *ortho* isomers in octa(aminophenyl)silsesquioxane (OAPS) from joint experimental characterizations and theoretical predictions of the IR and NMR spectra

**Saman Salimi,*[a] Farzaneh Radmanesh,[b] Nieck Benes,[b] Monika Pilz,[c] David Brown[a] and Sylvie Neyertz[a]**

[a]Univ. Savoie Mont Blanc, Univ. Grenoble Alpes, CNRS, Grenoble INP, LEPMI, 38000 Grenoble, France

[b]Membrane Science and Technology Cluster, Faculty of Science and Technology, MESA+ Institute for Nanotechnology, University of Twente, 7500 AE Enschede, The Netherlands

[c]SINTEF Industry, Forskningsveien 1, 0373 Oslo, Norway

## Highlights

- Octa(aminophenyl)silsesquioxane (OAPS) was obtained using two different synthesis routes
- The OAPS samples were compared using pycnometry, IR, 1D-NMR and 2D-NMR spectroscopy
- Database and DFT quantum mechanical predictions were used to complement the experimental characterizations
- Peaks in the IR, $^{13}$C-NMR and $^{1}$H-NMR spectra were clearly assigned to specific OAPS isomers

## Abstract

Polyhedral oligomeric silsesquioxane (POSS) compounds are defined by the chemical formula $(RSiO_{3/2})_8$ with R being an organic fragment. They display versatile features due to the combination of both their stable Si-O-Si inorganic cores and the large number of possible organic groups that can be attached to them. The present work aims at characterizing a highly-thermoresistant POSS, the octa(aminophenyl)silsesquioxane (OAPS). This siloxane-based cage has three different isomers

depending on the *meta*, *ortho* and *para* positions of the amines with respect to the phenyl groups and can be obtained using two synthesis routes. However, the presence of the isomers depends on the synthesis route and remains up to now an open question.

Experimental characterizations including pycnometry, infrared spectroscopy (IR), 1-dimensional and 2-dimensional nuclear magnetic resonance (NMR) have been performed for a commercial OAPS containing all three isomers and a controlled OAPS containing only the *para* and *meta* isomers. The density is found to be insensitive to the nature of the isomers, unlike the IR, $^{13}$C-NMR and $^{1}$H-NMR spectra that are isomer-dependent. To better identify the isomers, the experimental IR and NMR spectra were compared to predictions from Density Functional Theory (DFT) quantum mechanical methods and by machine-learning analyses. Within this context, quantum mechanical methods were found to be clearly superior to machine-learning methods, despite being computationally much more expensive. As a result, several peaks in the IR spectra and each peak in both the $^{13}$C-NMR and $^{1}$H-NMR spectra could be assigned to a specific OAPS isomer.


## Keywords

octa(aminophenyl)silsesquioxane (OAPS), *ortho*, *meta* and *para* isomers, IR and NMR spectroscopy, theoretical predictions


## Graphical abstract

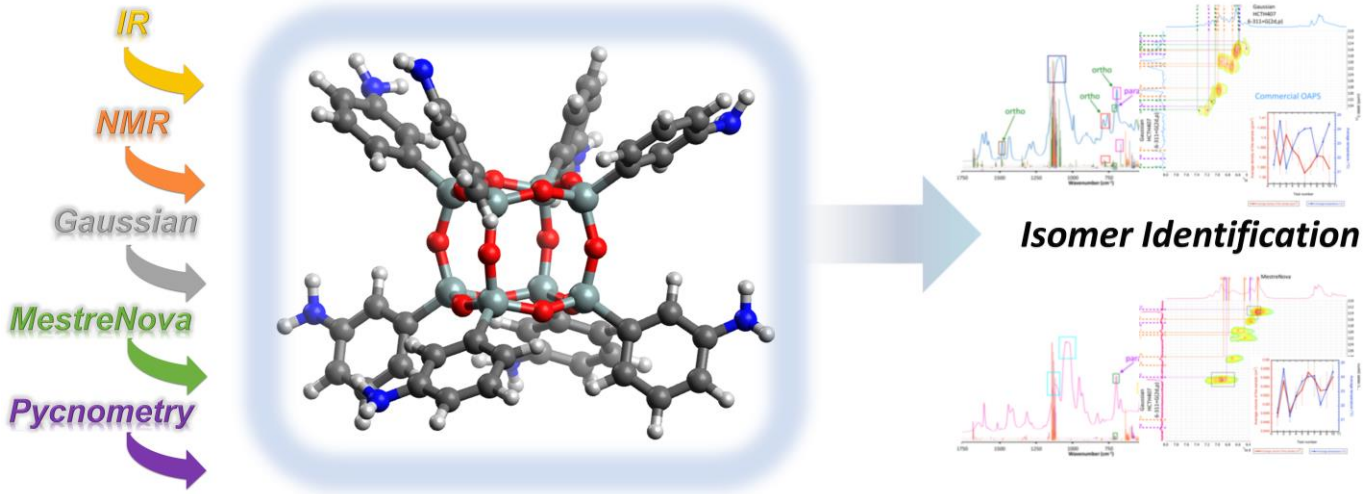

# Introduction

Compounds containing Si-O bonds have been studied for many years [1]. In the last two decades, the new field of silsesquioxane chemistry, based on the $RSiO_{3/2}$ repeat unit with R being an organic fragment, has gained interest. These hybrid materials display versatile features, which are due both to their potentially-reactive and easily-modified organic fragment and to their thermally-stable and chemically-inert Si-O-Si inorganic core. Various structures from ladder polymers to highly ordered species have been synthesized with the common formula $(RSiO_{3/2})_n$, with *n* being usually 6, 8, 10, 12 or 14 [2]. Those based on siloxane cages are called polyhedral oligomeric silsesquioxanes (POSS). They have nanoscale dimensions in the range of 1-3 nm depending on the organic substituent R along with a very robust inorganic framework [1].

In recent years, the incorporation of POSS into polymer matrices has attracted attention in order to create nanocomposites with enhanced mechanical and thermal properties [3]. Their rigid cage-like structure, nanoscale size and ability to tailor properties by introducing different functional groups make POSS effective candidates for high-performance membranes [4].

Octa(aminophenyl)silsesquioxane (OAPS) is a cubic POSS ($n$ = 8), in which the eight organic R substituents are phenyl moieties functionalized by primary amine groups. Its general chemical structure [5, 6] is displayed in Fig. 1, and because of its monosubstituted rings, it possesses three different isomers depending on the *meta*, *ortho* or *para* positions of the amine groups on the phenyl moieties. In addition, several isomers for the arms can coexist on the same cage. It has been shown experimentally that OAPS can have applications in the field of gas separation membranes [7-9]. Simulations have also been carried out on polyOAPS-imide membranes to investigate their molecular structures, thermomechanical stabilities and sorption properties [10, 11].

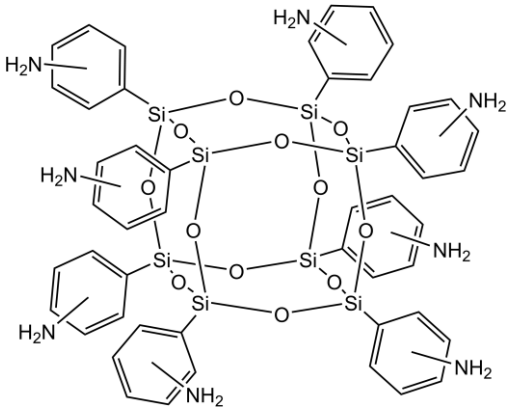

**Fig. 1.** The general structure of octa(aminophenyl)silsesquioxane (OAPS) [5, 6] The $NH_2$ group on each phenyl ring can either be in the *meta*, *ortho* or *para* position.

OAPS can be obtained using two main synthesis routes. The first and most common one is Laine's method (Fig. S1) [5, 12-18] leading to OAPS cages with the organic moieties on the same cage being probably in different forms (e.g. a cage can have five -$NH_2$ groups in the *meta* position, two in the *ortho* position, and one in the *para* position, and so on). As shown in Fig. S1, it starts with nitration of octa(phenyl)silsesquioxane (OPS), which results in octa(nitrophenyl)silsesquioxane (ONPS) as an intermediate product and is subsequently reduced to OAPS. Using this method, Tamaki et al. [5] reported the presence of almost equal *meta* and *para* isomers for OAPS, without any *ortho* isomer due to the steric and electron-withdrawing effects of the silsesquioxane core. By cleaving the Si-C bonds, Kim et al. [14] indicated that the *ortho* isomer is also present and reported the ratios as being 70%, 25% and 5% for *meta*, *ortho* and *para*. Takahashi et al. [15] obtained 76%, 21% and 3% for the same combination. Sulaiman et al. [19] reported 65%, 10% and 25% for the *meta*, *ortho* and *para* isomers of ONPS, respectively, which likewise indicated the presence of the three isomers in this OAPS precursor.

The other route, which is less used, is Lee's method (Fig. S2) [20]. Rather than modifying OPS as in Laine's method, Lee's route is an isomer-controlled approach, which starts directly from the aminophenyltrimethoxysilane (APTMS) precursors for the aminophenylsilsesquioxane (APS) structures. To our knowledge, this was only attempted with the *meta* and *para* isomers of APTMS (Fig. S2) [20]. The separate pure *meta*-APS and *para*-APS each led to a mixture of cage sizes ranging from 8 to 14 $RSiO_{3/2}$ units. This alternative approach thus allows for a better control of the isomer forms, but its disadvantage is that the cage sizes are less well-controlled than with Laine's nitration/reduction of OPS.

As noted above, Laine's method is by far the most common route used. However, there are uncertainties and disagreements on the nature of the isomers present in the products resulting from the nitration/reduction approach and, since OAPS is intended as a building block for nanocomposites, this is

likely to have important consequences on the potential applications [10, 11]. In the present work, we attempt to identify the signature of the isomers using traditional characterization techniques such as density, IR and NMR. They are carried out on two different sources of OAPS, i.e. one from Laine's method and one from Lee's method. The experimental results are further complemented by predictions from machine-learning approaches, as implemented in the MestreNova software [21], and from Density Functional Theory (DFT) quantum mechanical approaches, as used in the Gaussian software [22], in order to identify the specific IR and NMR peaks for the *meta*, *ortho* and *para* isomers of OAPS.

# Materials and methods

**A. Materials**. The "commercial OAPS" was bought in the form of an off-white powder from Gelest Inc. [6] and is produced via Laine's method [5]. It was presented as containing all three isomers. The "controlled OAPS" was synthesized from an adaptation of Lee's controlled conversion method [20] using DMSO at elevated temperatures and under alkaline conditions upon accelerated hydrolysis and condensation of a mixture of *meta* (30-40%) and *para* (60-70%) APTMS purchased from Gelest Inc. The final product is a 21% w/w solution of *para* and *meta* isomers of OAPS dissolved in DMSO.

The main structural differences between the commercial and controlled OAPS can be summarized as follows:

1) the commercial OAPS should contain all three isomers
2) the controlled OAPS should not have any *ortho* isomer
3) the controlled OAPS contains a lot more of the *para* isomer than the commercial OAPS
4) the commercial OAPS should be based solely on eight-cornered siloxane cages, while there could be larger siloxane cage structures too in the controlled OAPS.

**B. Pycnometry**

Density measurements were carried out by an AccuPyc II 1340 gas displacement density analyzer (Micromeritics), with helium as the probe gas. Pycnometry is non-destructive as it uses the gas displacement method to measure the volume. It generates much more precise and reproducible densities than the traditional Archimedes water displacement method [23] since the small gas atoms can diffuse in the cavities and any open space. The precision is guaranteed within ± 0.015 $cm^3$ for this pycnometer of cell chamber volume 74.051 $cm^3$ [23].

Following calibration tests, about 1 g of OAPS sample was placed in a vacuum oven to evaporate any moisture. It was then weighed and transferred rapidly into the pycnometer to limit as much as possible the reabsorption of humidity. Ten purges and thirty cycles were set for each test, and ten tests

were repeated for each sample to account for the variation in the ambient temperature. The pycnometer calculates the volume of the sample, $V_{sample}$ by using Equation 1 [23]:

$$V_{sample} = V_{cell} - \frac{V_{expansion}}{\frac{P_1}{P_2} - 1} \quad (1)$$

where $P_1$ is the gauge pressure after filling by helium and $P_2$ is the gauge pressure after expansion. $V_{cell}$, i.e. the cell volume, and $V_{expansion}$, i.e. the expansion volume, are already known via a calibration procedure. $P_1$ and $P_2$ are measured by the gauge included inside the pycnometer. The density is obtained from $V_{sample}$ and the weight of the sample measured by using a high-precision balance.

**C. IR spectroscopy**

The IR spectra for the OAPS samples were obtained with a Spotlight 400 Perkin Elmer ATR-IR spectrometer. The powder was directly used to perform the analysis for the commercial OAPS. Since the controlled OAPS was initially dissolved in DMSO, its solvent was first evaporated before performing the IR analyses.

**D. NMR spectroscopy**

The one-dimensional $^{13}$C-NMR and $^{1}$H-NMR, as well as the two-dimensional $^{13}$C/$^{1}$H-NMR spectra, were recorded for the OAPS samples dissolved in DMSO-d6 by using a Bruker AVANCE Neo 600 MHz NMR spectrometer.

**E. Machine-learning MestreNova software for NMR predictions**

MestreNova [21] is a spectral data analyzing and predicting software produced by Mestrelab Research, which includes a module called "NMRPredict". The most common algorithms for NMR prediction use reference databases where a large number of spectra and their assigned 2D or 3D chemical structures are the source knowledge. MestreNova uses both machine learning and the HOSE (Hierarchical Organization of Spherical Environments) code prediction for structures that are represented in its reference collection [21, 24]. It also uses a Neural Network algorithm for atoms whose environments are not in its database [21].

MestreNova includes a built-in module for minimization of the input structures and it provides a choice of common solvents, i.e. DMSO in this case. MestreNova was used separately on the three pure isomers of OAPS to predict their specific NMR shifts For each isomer, four separate model molecular structures were prepared and fed to MestreNova to perform their optimization and the NMR predictions. An optimized structure obtained by MestreNova is shown for each isomer in Fig. S3.

### F. Quantum mechanical Gaussian software for IR and NMR predictions

Gaussian performs quantum mechanical calculations to predict molecular structures, energies and spectroscopic data [22, 25-28]. The *ab initio* methods, such as Hartree-Fock (HF), which investigate all the details of the electron movements are computationally very expensive. However, many properties of a molecule can be derived from its electron density distribution only [29, 30], which gave rise to the faster DFT approaches [30].

For predicting both the geometries and the IR vibrational bands, DFT calculations [31] were carried out with the Gaussian 09 code [22] at the B3LYP/6-31G(d,p) level of theory on four separate model structures for each of the pure *para*, *meta* and *ortho* isomers of OAPS. B3LYP is a hybrid density functional with the polarization functions added to a double-zeta basis set 6-31G(d,p) [32-36], and it has been shown to be a very good compromise between calculation time and accurate energy minimisation [32, 35-37]. The Avogadro software [38, 39] was used to identify the IR vibrational modes calculated by Gaussian.

In the case of the NMR peaks, predicted chemical shielding can be very dependent on the level of theory used. To do an in-depth study, different DFT functionals for NMR predictions [40-43], *i.e.* B3LYP [44-50], B3PW91 [41, 51-55], and HCTH407 [51, 56-58] were used along with the accurate 6-311+G(2d,p) basis set [43, 53, 59, 60] when using the Gaussian code. Preliminary tests were carried out with the lower 6-31G(d,p) basis set but were not satisfactory. The SCRF (Self-Consistent Reaction Field) keyword [61] was added to account for the presence of the solvent (here, DMSO) by locating the solute in a cavity within the solvent reaction field using the Polarizable Continuum Model (PCM) [22, 62-74]. The GIAO (Gauge-Including Atomic Orbital) formulation resulted in all matrix elements involving the basis functions being independent of the origin [75]. In a first step, four structures for each isomer were prepared using the Hyperchem software [76], fed to Gaussian and optimized at the B3LYP/6-31G(d,p) level of theory (see Fig. S4). In a second step, their $^{13}$C-NMR and $^{1}$H-NMR spectra were predicted using B3LYP, B3PW91 and HCTH407 at the 6-311+G(2d,p) level of theory. Since Gaussian calculates the absolute shieldings, the same level of theory had to be used for tetramethylsilane (TMS) as the reference for the chemical shifts [53].

Quantum mechanical calculations are in general very costly in terms of calculation time to complete both optimization and NMR predictions, whereas MestreNova produces the results within a few minutes. As such, it is interesting to attempt and compare both approaches.

## Results and discussion

## 1. Pycnometry

Fig. 2a and Fig. 2b show the details of the volumes and densities (red continuous lines) measured over 10 tests for the commercial OAPS sample, along with the specific test temperatures (blue dashed lines). The volume and density of the commercial OAPS change by 0.0032 $cm^3$ and 0.0069 $g/cm^3$ per °C, respectively. The density of the commercial OAPS sample averaged over the ten tests was found to be 1.39 $g/cm^3$ with a standard deviation of 0.01 $g/cm^3$. Similarly, the density of the controlled OAPS sample was found to be 1.37 $g/cm^3$ with a standard deviation of 0.01 $g/cm^3$. The density thus seems fairly insensitive to the presence and proportions of the isomers.

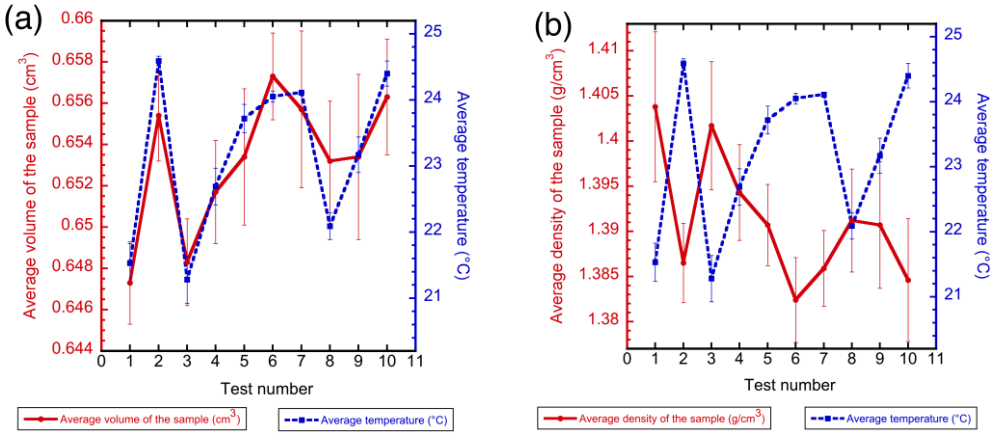


**Fig. 2.** The average temperature along with (a) the average volume and (b) the average density of the commercial OAPS recorded over ten pycnometry tests.

## 2. IR spectroscopy

### 2.1. Experimental spectra

Since the IR spectra arise from changes in dipole moments, different isomers with different proportions of symmetry may present different spectra, i.e. the change in the dipole moment may diminish in a more symmetrical structure such as the *para* isomer. Indeed, Fig. 3 shows that there are differences between the experimental spectra of (a) the commercial OAPS and (b) the controlled OAPS. There are no signs of large peaks around 3500 $cm^{-1}$, which would be characteristic of -OH groups and thus of open siloxane cages. This suggests that most parts or all of the cages are intact (closed cages).

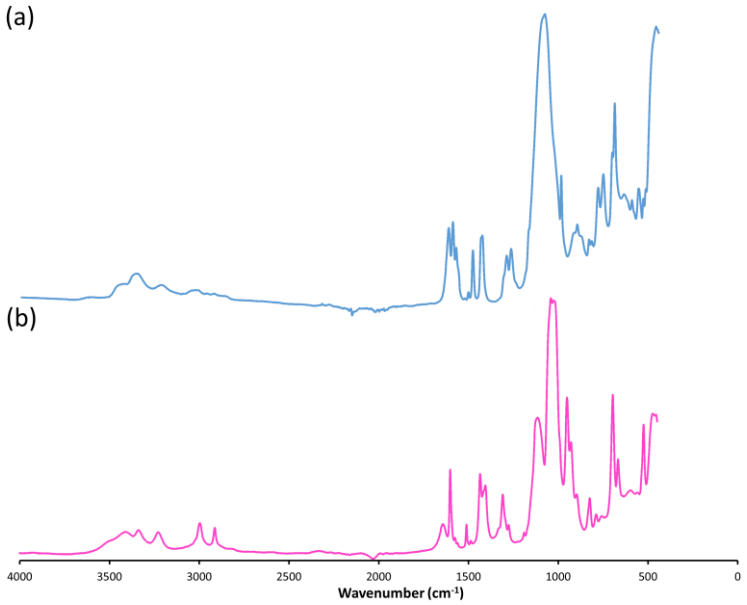


**Fig. 3.** The experimental IR spectrum for (a) the commercial and (b) the controlled OAPS

### 2.2. IR Predictions

As noted above, the IR vibrational bands were predicted with Gaussian using DFT calculations at the B3LYP/6-31G(d,p) level of theory on optimized model structures of the pure isomers. When comparing experimental $\tilde{\nu}_{exp}$ and predicted $\tilde{\nu}_{calc}$ wavenumbers, differences can arise due to errors related to the method, the anharmonicity, the solvent effects, the Fermi resonance, etc [77]. The errors can be reduced by using a scaling equation [77] obtained from plotting the predicted wavenumbers versus their corresponding experimental values. The linear correlation ($R > 0.9998$) between the $\tilde{\nu}_{calc}$ of seven clearly-defined vibrations for the *meta*-OAPS isomer and the $\tilde{\nu}_{exp}$ for the commercial sample is displayed in Fig. 4.

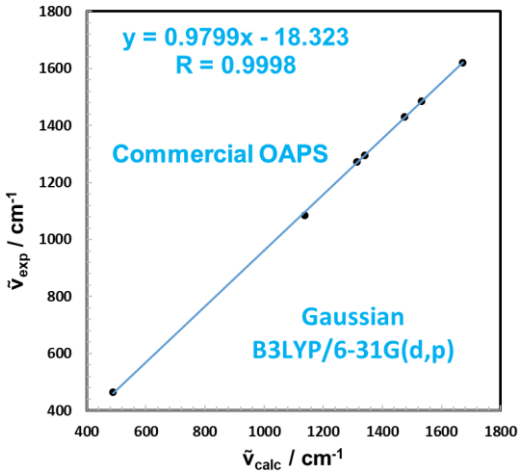


**Fig. 4.** The DFT-predicted $\tilde{\nu}_{calc}$ at the B3LYP/6-31G(d,p) level of theory for *meta*-OAPS versus the corresponding $\tilde{\nu}_{exp}$ in the commercial OAPS sample.

If $|e_i|$ are the absolute errors between the predicted and their corresponding experimental data and $n$ is the number of data, the mean absolute error (MAE) and root mean square error (RMSE) can be calculated from [78]:

$$\text{MAE} = \frac{1}{n}\sum_{i=1}^{n}|e_i| \tag{2}$$

$$\text{RMSE} = \sqrt{\frac{1}{n}\sum_{i=1}^{n}e_i^2} \tag{3}$$

As shown in Table 1, the errors are dramatically reduced after scaling the $\tilde{\nu}_{calc}$ by the equation shown in Fig. 4. The MAE and RMSE decrease from 44 $cm^{-1}$ and 45 $cm^{-1}$ to 3.7 $cm^{-1}$ and 5.2 $cm^{-1}$, respectively. The correlation coefficient in Fig. 4 is also compatible with that reported by Alcolea et al. for calculations at the B3LYP/6-31G(d,p) level of theory [77].

**Table 1.** Comparison between the predicted $\tilde{\nu}_{calc}$ for *meta*-OAPS, the experimental $\tilde{\nu}_{exp}$ in the commercial OAPS and the scaled $\tilde{\nu}_{calc\_scaled}$ wavenumbers in $cm^{-1}$ along with their absolute error $|e_i|$ in $cm^{-1}$.

| $\tilde{\nu}_{calc}$ | $\tilde{\nu}_{exp}$ | $\tilde{\nu}_{calc\_scaled}$ | $\lvert e_i\rvert_{exp\text{-}calc}$ | $\lvert e_i\rvert_{exp\text{-}calc\_scaled}$ |
|---|---|---|---|---|
| **489** | 464 | 461 | 25 | 3 |
| **1137** | 1084 | 1096 | 53 | 12 |
| **1313** | 1272 | 1268 | 41 | 4 |
| **1340** | 1296 | 1295 | 44 | 1 |
| **1475** | 1431 | 1427 | 44 | 4 |
| **1532** | 1484 | 1483 | 48 | 1 |
| **1672** | 1619 | 1620 | 53 | 1 |

Fig. 5 compares separately the DFT-predicted and scaled vibrations for the (a) *meta*, (b) *ortho* and (c) *para* isomers with the experimental IR spectra of the commercial OAPS (Fig. 3a) along with the specific identification of the various vibrational modes obtained by using the Avogadro software. The predicted spectra are obviously restricted to specific optimized structures while the experimental spectrum takes into account the very large number of possible structures, hence its much broader peaks.

However, Fig. 5a for the *meta* isomer still indicates a good compatibility between the experimental and the predicted spectra for wavenumbers below 1700 $cm^{-1}$. The predicted bands for the *ortho* isomer (Fig. 5b) are broader, especially for the Si-O-Si stretching vibrations. Fig. 5c for the *para* isomer indicates lower intensities for most of the predicted bands due to its more symmetrical structure. This suggests that there are indeed higher proportions of the *ortho* and *meta* isomers in the commercial OAPS. All three predicted spectra show slightly overestimated bands for wavenumbers beyond 3000 $cm^{-1}$, but such overestimations for the N-H vibrations have already been observed elsewhere [79-83] and this is a part of the spectrum which has very low intensities.

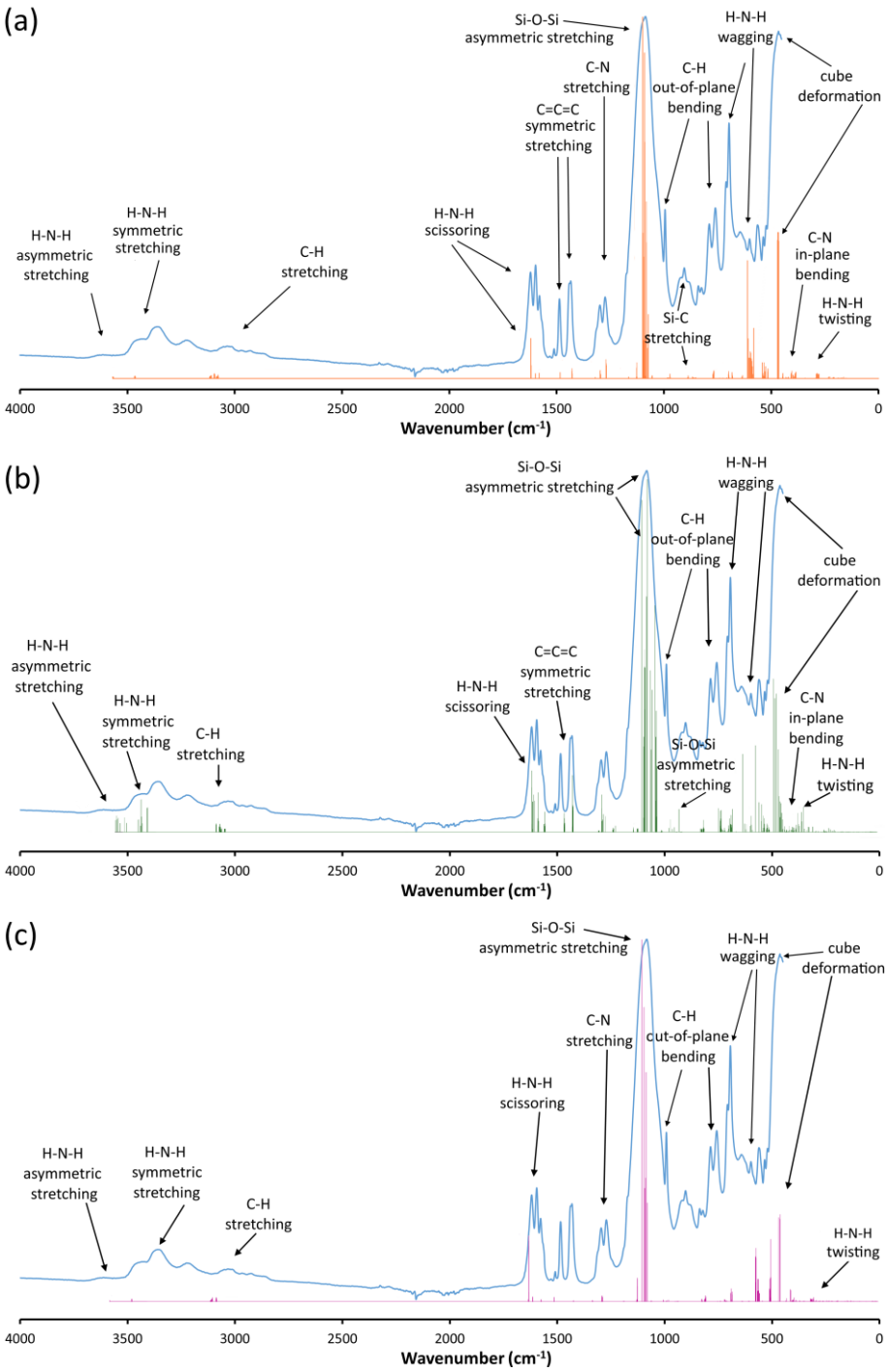


**Fig. 5.** A comparison of the experimental IR spectrum for the commercial OAPS (blue) with the predicted and scaled vibrations for model (a) *meta* (orange), (b) *ortho* (green), and (c) *para* (purple) pure isomers of OAPS obtained from DFT calculations at the B3LYP/6-31G(d,p) level.

Fig. 6 compares the experimental spectra of both (a) the commercial and (b) the controlled OAPS with the three predicted and scaled IR spectra assembled. Several isomer-specific information can be obtained:

- The compatibility between the experimental and the three predicted spectra assembled is rather good for the commercial OAPS, which seems to agree with the presence of the *ortho* isomer, despite what has been reported by Tamaki et al. [75].

- A sharp peak of H-N-H wagging at 520 $cm^{-1}$ (yellow rectangle) is observed for the controlled OAPS while there is only a small trace of it for the commercial one. Unlike for the other isomers, this rather strong peak was predicted for the *para*-OAPS, which could confirm its high proportion in the controlled OAPS.

- Two strong peaks for the out-of-plane vibrations of C-H appear at 756 $cm^{-1}$ and 784 $cm^{-1}$ (red rectangle) for the commercial OAPS, whereas they almost disappear for the controlled OAPS. Both of them correspond to predicted bands for the *ortho* isomer.

- The strong peak at 1115 $cm^{-1}$ (dark blue rectangle) in the commercial OAPS illustrates the Si-O-Si stretching vibrations which are common to the three isomers [84]. In the controlled OAPS, this broad peak is split into two peaks (light blue rectangles) for the *meta* and the *para* isomers, with only one overlapping with the predicted peaks. As such, it is not easy to assign these peaks to a specific isomer but it is clear that the *ortho* isomer in the commercial OAPS leads to broader predicted bands in this region.

- The sharp peak at 1485 $cm^{-1}$ for the commercial OAPS (brown rectangle) corresponds to a predicted band for the *ortho*-OAPS and does not appear in the controlled OAPS.

- The predicted bands for the *ortho*-OAPS from 1280 $cm^{-1}$ to 1690 $cm^{-1}$ are stronger than for the other two isomers (see Fig. 5b). This agrees with the experimental spectrum of the commercial OAPS showing stronger peaks in the same region than the controlled one.

- Other peaks could be specific to one isomer, although many of them overlap in the experimental spectra. For example, the peak appearing at 670 $cm^{-1}$ (pink rectangle) in the commercial OAPS seems to correspond to the *ortho* isomer. The peak at 710 $cm^{-1}$ (green rectangle), which is sharp in the controlled OAPS matches with a predicted peak for the *para*-OAPS.

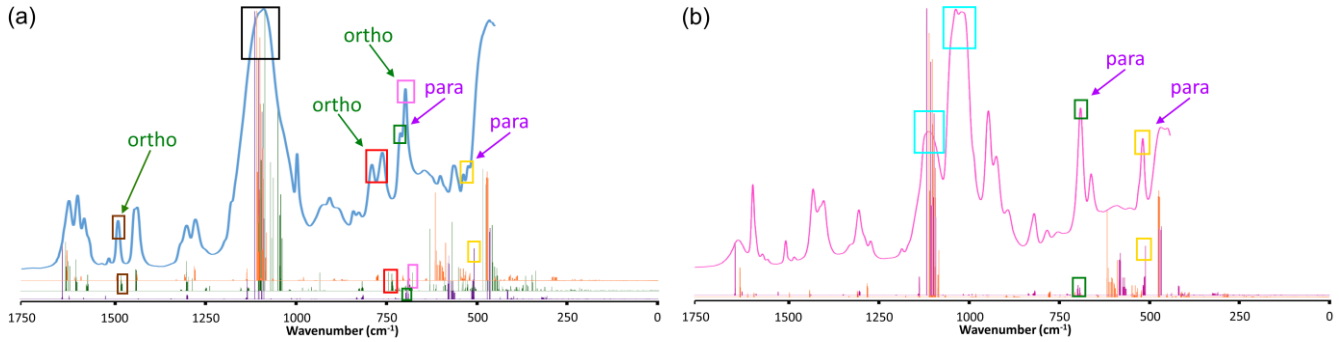


**Fig. 6.** A comparison of (a) the commercial (blue) and (b) the controlled (pink) OAPS experimental spectra with the predicted and scaled IR spectra for the *meta* (orange), *ortho* (green), and *para* (purple) OAPS isomers up to 1750 $cm^{-1}$.

These compared analyses seem to confirm the different natures of both OAPS samples in terms of isomer mixtures and show how DFT predictions on a limited number of model structures can be a useful tool to help for the interpretation of the experimental spectra.

## 3. NMR spectroscopy

### 3.1. Experimental spectra

NMR characterizations were initially attempted for $^{29}Si$, $^{13}C$ and $^{1}H$. In the experimental $^{29}Si$-NMR spectra, all the peaks fell within a very restricted ppm range, it was not possible to find a specific experimental signature of the *ortho* isomer, and the prediction methods tested were unable to provide an unambiguous distinction of the isomers [85]. In addition, the main peak of the $^{29}Si$-NMR spectra for the pure *para* isomer reported by Lee et al. [20] did not agree with the experimental $^{29}Si$-NMR spectra measured on the samples dissolved in DMSO-d6. So there were issues in both the predicted [85] and experimental [20] $^{29}Si$-NMR shifts. However, it was found that the one-dimensional and two-dimensional $^{13}C$-NMR and $^{1}H$-NMR spectra were sufficient to clearly identify the isomers. Consequently, only these latter NMR characterizations will be presented here.

Fig. 7 shows the good compatibility of the $^{13}C$-NMR spectrum for (a) the commercial OAPS (light blue line) with that of (c) OAPS produced through nitration/reduction by Krishnan et al. (dark blue line) [86]. There are at least two peaks at 132 ppm and 154 ppm in the nitration/reduction samples (green rectangles), that have no equivalent peaks in the (b) controlled OAPS spectrum (pink line). These two peaks should be related to the presence of the *ortho* isomer. Surprisingly, there is a peak in (b) (red rectangle) that shows such a small trace that it cannot be easily revealed in the nitration/reduction samples. It could correspond to the *para* isomer as it is stronger in the controlled OAPS $^{13}C$-NMR

spectra. That may be why Tamaki et al. [5] reported only ten observable peaks for their nitration/reduction $^{13}$C-NMR OAPS spectrum and concluded that this reflected the presence of the *meta* and *para* isomers only. However, there are definitely indications of the presence of the *ortho* isomer too in samples obtained by Laine's method.

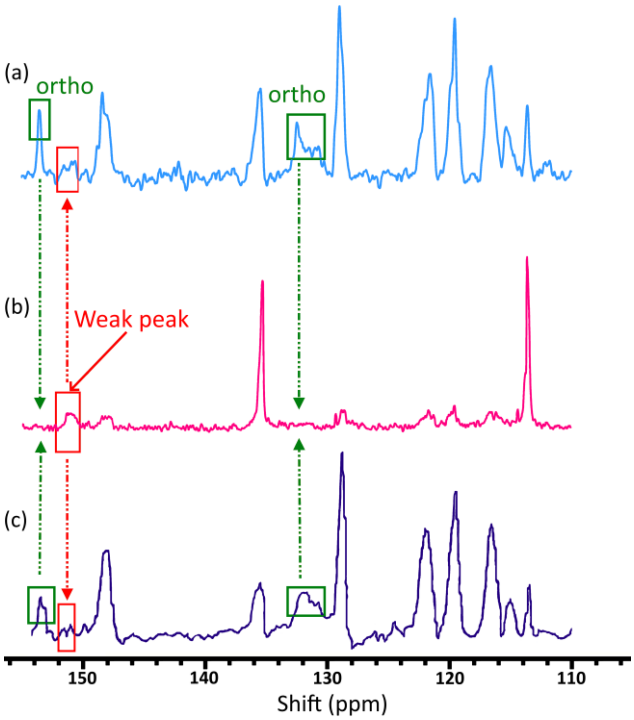


**Fig. 7.** A comparison of the experimental $^{13}$C-NMR spectra for (a) the commercial OAPS, (b) the controlled OAPS and (c) the OAPS prepared by Krishnan et al. [86], all of them in DMSO-d6, along with a proposed assignment for *ortho*-specific peaks.

The $^{1}$H-NMR spectra of the commercial and controlled OAPS are compared to that obtained by nitration/reduction by Zhang et al. [87] in Fig. 8. Both commercial (light blue line) and Zhang (dark blue line) OAPS spectra are again quite similar but different from the controlled OAPS spectrum (pink line). They are also compatible with the $^{1}$H-NMR spectra published by Tamaki et al. [5] and Huang et al. [84]. Two broad regions can be distinguished: one from 4.2 ppm to 5.4 ppm, which corresponds to the amine hydrogens, and the other one from 6.2 ppm to 7.8 ppm, which is related to the four aromatic hydrogens of the OAPS phenyl moieties. The latter appears in a slightly more narrow range, i.e. 6 ppm to 7.3 ppm, for the controlled OAPS. The main differences between the spectra are:

- The yellow rectangles at 5.3 ppm, red rectangles at 6.6 ppm and green rectangles at 7.3 ppm show peaks that do not appear in the (b) controlled OAPS spectrum and can thus be linked to the *ortho* isomer.

- The orange rectangles at 5.15 ppm indicate small peaks in both (a) the commercial and (c) Zhang OAPS, which become stronger for the (b) controlled OAPS with a higher proportion of *para* isomer. Similarly, the sharp peak at 6.25 ppm in the controlled OAPS (brown rectangle) is probably also related to the aromatic *para* hydrogens.

The number of amine functional groups on each ring connected to the siloxane cage can be obtained by dividing the integrated area underneath the peaks. This ratio is equal to 2 for all OAPS under study, which means that there are two amine hydrogens along with four aromatic hydrogens, i.e. one $-NH_2$ per ring for all three samples. However, it is difficult to distinguish the aromatic hydrogens of the different OAPS isomers. This is the reason why Tamaki et al. [5] tried to use the $^1$H-NMR spectrum of ONPS, which has sharper peaks, in order to calculate the isomer ratios.

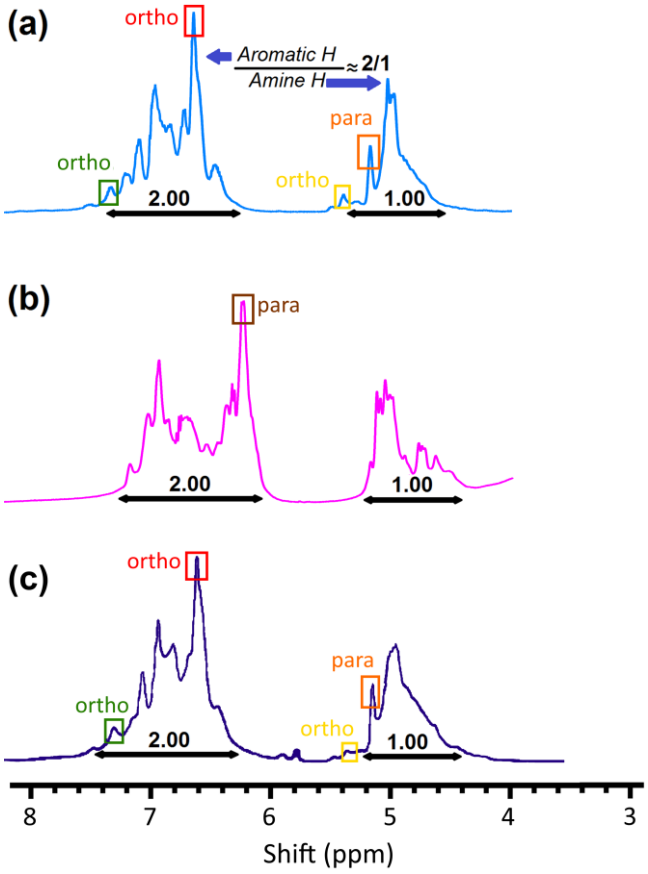


**Fig. 8.** A comparison of the experimental $^1$H-NMR spectra and surface areas of (a) the commercial OAPS, (b) the controlled OAPS, and (c) the OAPS prepared by Zhang et al. [87], all of them in DMSO-d6, along with a proposed isomer assignment for the main peaks.

In a two-dimensional (2D) heteronuclear single-quantum correlation (HSQC) spectrum, the 1D-NMR of one nucleus is plotted versus the 1D-NMR of another type of nucleus [88]. Here, the HSQC spectra correlate the $^{13}$C and $^1$H spectra to each other. To interpret such a spectrum, each $^{13}$C shift is

selected on the *y*-axis and a line is drawn horizontally until a cross-peak is encountered. Similarly, each $^{1}$H shift is selected on the *x*-axis and a line is drawn vertically until a cross-peak is encountered. These cross-peaks identify which hydrogens are connected to which carbons and vice versa. When a line encounters no cross-peak, it implies that this carbon has no connected hydrogen.

Fig. 9(a) shows the HSQC spectrum obtained for the commercial OAPS. Ten cross-peaks can be observed, indicating ten different carbons connected each to one hydrogen. It confirms that the $^{1}$H-NMR shifts from 6.2 ppm to 7.8 ppm refer to the aromatic hydrogens. The three isomers of the commercial OAPS possess sixteen different environments for carbon atoms, ten of which are connected to the hydrogens and the six others to either silicons or nitrogens. The black rectangle shows the $^{1}$H-NMR signals presenting no connections to the carbon atoms. These peaks between ~4.5 ppm to ~5.5 ppm are the amine hydrogens, as reported by Tamaki et al. [5]. The brown rectangle indicates a $^{1}$H-NMR shift specific to the *ortho* amine hydrogens (Fig. 8), likewise, the green rectangles, which indicate *ortho*-specific $^{13}$C-NMR shifts (Fig. 7). The orange and purple rectangles show the $^{13}$C-NMR signals displaying no connections to the hydrogens. The yellow rectangles for $^{1}$H and red rectangles for $^{13}$C give examples of overlapping peaks. The blue rectangles indicate points, which are probably related to impurities. Such an HSQC spectrum clearly confirms the presence of the three isomers and suggests that the analysis of Kim et al. [14] is more accurate than that of Tamaki et al. [5].

Fig. 9b shows the HSQC spectrum of the controlled OAPS. Six cross-peaks corresponding to six different carbons connected each to one hydrogen can be observed, as expected from the presence of the *meta* and *para* isomers only. The four remaining carbons are those connected to either silicon or nitrogen. The purple rectangle shows again the $^{13}$C-NMR signals having no connections to the hydrogens. The $^{1}$H-NMR peaks between ~4.5 ppm to ~5.5 ppm are the amine hydrogens as indicated by the brown rectangle. The specific *ortho* amine shift is absent from Fig. 9b. The pink rectangles display expanded cross-points, which could be related to the different sizes of the OAPS cages in the controlled sample. Indeed, different cages sizes possess different numbers of oxygens and as such, they probably have slightly different electron-withdrawing tendencies. The $^{13}$C-NMR peaks specific to the *ortho* isomer (Fig. 9a) disappear in Fig. 9b, thus confirming its absence. This specific HSQC spectrum shows that there are indeed only two isomers out of the possible three in the controlled OAPS sample.

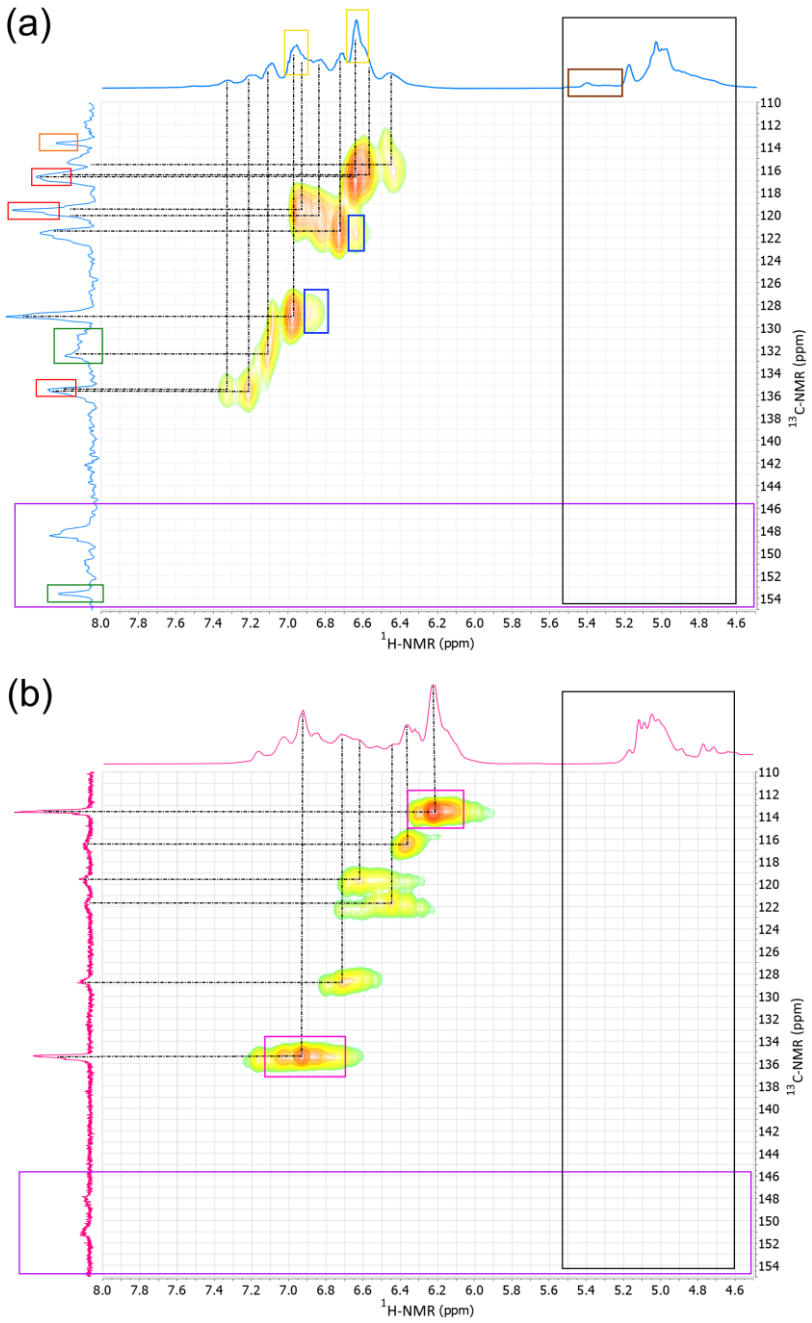


**Fig. 9.** The HSQC spectra of (a) the commercial OAPS and (b) the controlled OAPS.

While comparisons of the experimental spectra allow identifying a few of the isomer-specific peaks (Figs. 7-9), most peaks cannot be interpreted unambiguously. As such, the experimental characterizations were completed by NMR predictions. Indeed the latter are known as being a powerful tool to accomplish tough tasks such as the structural assignment of organic molecules, which are difficult by the conventional observational methods on their own [53, 89-96]. However, NMR predictions are unfortunately dependent on the type of method and level of theory used, due to different sources such as electron correlations and vibrational effects [43, 97-99]. As such, the predictions first need (if possible) to

be compared to the available experimental spectra in order to identify which prediction methods are the most accurate.

### 3.2. Case study for prediction: the *meta*-OAPS isomer

Due to the highly time-consuming DFT calculations, only the *meta-OAPS* isomer (Fig. 10) was first fed to both MestRenova and Gaussian in order to compare their predicted chemical shifts.

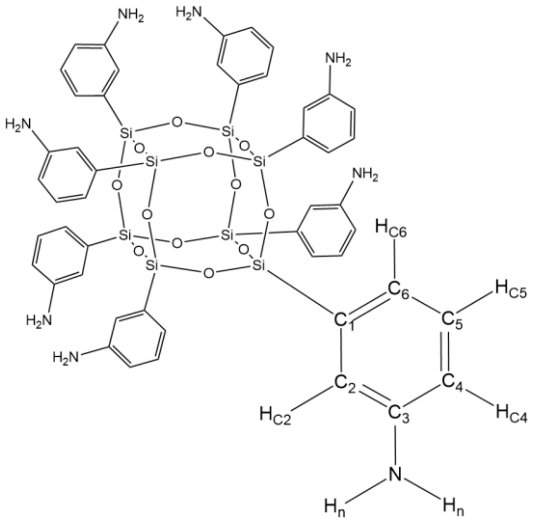


**Fig. 10.** The molecular structure of *meta*-OAPS. The lower ring is expanded to show the names of the phenyl ring aromatic carbons and hydrogens as well as the amine groups.

#### 3.2.1. *The $^{13}$C-NMR predicted spectra for meta-OAPS*

Fig. 11 shows the predicted specific $^{13}$C-NMR shifts for *meta*-OAPS using different methods and levels of theory along with the experimental spectrum for the commercial OAPS. No overlaps are predicted by either MestRenova or Gaussian.

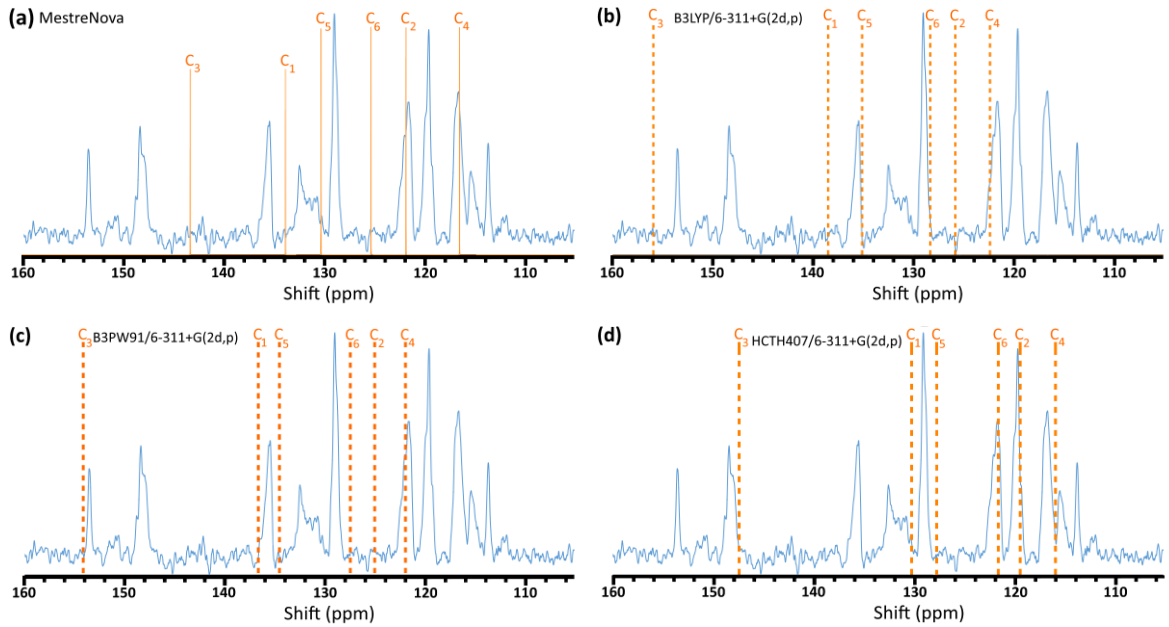


**Fig. 11.** A comparison of the commercial OAPS $^{13}$C-NMR experimental spectrum (blue line) with the chemical shifts predicted for the aromatic carbons of *meta*-OAPS by (a) MestreNova (lines) and (b-d) Gaussian (dashed lines) using different DFT functionals along with the 6-311+G(2d,p) basis set.

As the four predicted spectra are not easy to distinguish, the quality of the prediction was assessed by calculating the differences between all predicted peaks and their closest experimental peaks according to Equation 4. To eliminate the background, only the experimental peaks whose intensity was at least 25% of the main peak at 129 ppm were selected. This allowed for the comparison of all predicted spectra under the same conditions.

$$Difference = \sqrt{\sum (\text{predicted shift - closest experimental shift})^2} \tag{4}$$

Differences in ppm are reported in Table 2 for the various methods tested and show that DFT at the HCTH407/6-311+G(2d,p) level of theory gives the best prediction for the *meta*-OAPS. As such, it will be the method used to predict the $^{13}$C-NMR shifts for the *ortho* and *para* isomers.

**Table 2.** The differences between the experimental and the predicted $^{13}$C-NMR peaks for *meta*-OAPS according to Equation 4. The three DFT calculations were carried out at the 6-311+G(2d,p) level of theory.

| **Method** | MestRenova | B3LYP | B3PW91 | HCTH407 |
|---|---|---|---|---|
| **Difference / ppm** | 2.5 | 2.3 | 2.1 | 1.4 |

### 3.2.2 *The $^{1}$H-NMR predicted spectra for the meta-OAPS*

Fig. 12 shows the predicted $^{1}$H-NMR spectra for *meta*-OAPS using different prediction methods and levels of theory along with the commercial OAPS experimental spectrum. As a whole, the (a) MestreNova predictions match well with the experimental data. On the contrary, the three DFT methods (b-d) overestimate the chemical shifts for the aromatic hydrogens (with the pink rectangles showing possible overlaps) and underestimate the chemical shifts for the amine hydrogens. The same problem for amines was reported earlier [100, 101] and was attributed to $NH_2$ groups forming hydrogen bonds with the solvent (here, DMSO-d6), which is not properly taken into account by the PCM formalism [101, 102].

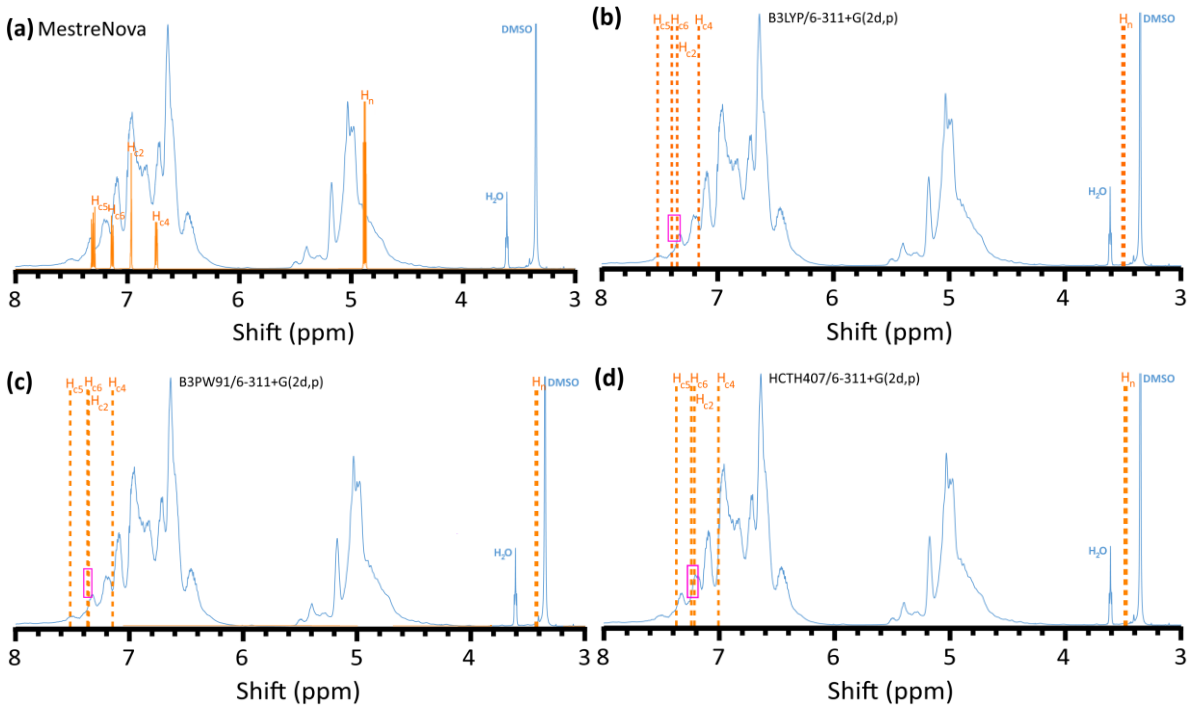


**Fig. 12.** A comparison of the commercial OAPS $^{1}$H-NMR experimental spectrum (blue line) with the chemical shifts predicted for the aromatic and amine hydrogens of *meta*-OAPS by (a) MestreNova (lines) and (b-d) Gaussian (dashed lines) using different DFT functionals along with the 6-311+G(2d,p) basis set.

Since it is more difficult to assign each predicted $^{1}$H-NMR shift to a specific experimental one than for $^{13}$C-NMR (Equation 4 and Table 2), the methods were here compared based on the distance between the lowest shift for the aromatic H and the sharpest experimental peak at 6.64 ppm (Table 3). MestreNova gives the best prediction but HCTH407/6-311+G(2d,p) is again the most appropriate DFT approach. As it would be better to be able to predict all types of spectra with the same method, it was decided to further prospect the $^{1}$H-NMR OAPS spectra using both MestreNova and HCTH407/6-311+G(2d,p) in order to predict the *ortho* and *para* $^{1}$H-NMR spectra in addition to that of the *meta* isomer.

**Table 3.** The differences between the main experimental and the closest predicted $^{1}$H-NMR peaks for the aromatic hydrogens of the *meta*-OAPS. The three DFT calculations were carried out at the 6-311+G(2d,p) level of theory.

| **Method** | MestRenova | B3LYP | B3PW91 | HCTH407 |
|---|---|---|---|---|
| **Difference / ppm** | 0.01 | 0.51 | 0.50 | 0.17 |

### 3.3. NMR predictions for all three isomers

As for the *meta* isomer (Fig. 10), Fig. 13 shows the different chemical environments for the carbons and hydrogens of the *ortho* and *para* isomers of OAPS.

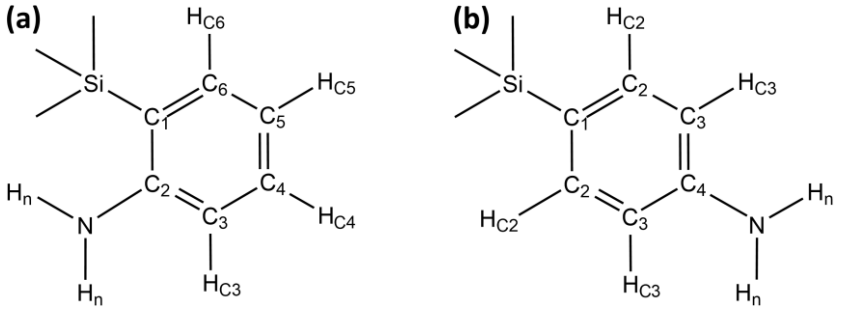


**Fig. 13.** A close-up of the molecular structures of a) the *ortho* and b) the *para* isomer arms connected to the siloxane cage showing the names of the phenyl ring aromatic carbons and hydrogens as well as the amine groups

In the following part, all the results were averaged over four separate starting structures for each isomer. It was first checked that the results for each separate structure were similar [85]. They were indeed found to be reproducible: the range for the predicted $^{13}$C-NMR shifts for a specific atom was within less than 2 ppm, while that for specific $^{1}$H-NMR shifts was within less than 0.2 ppm.

#### 3.3.1. *The $^{13}$C-NMR predicted spectra for all three isomers*

The average $^{13}$C-NMR spectra for all three isomers predicted using DFT at the HCTH407/6-311+G(2d,p) level of theory are compared in Fig. 14 to those of the experimental (a) commercial and (b) controlled samples. As before, the predicted peaks are identified by their colours with orange representing the *meta* isomer, green representing the *ortho* isomer and purple representing the *para* isomer.

In Fig. 14a, the predicted *ortho* green shift at 111.5 ppm (P) matches a weak experimental peak for the commercial OAPS sample. A similar match can be observed for two *para* purple shifts at 117.5 ppm (K) and 149.5 ppm (B). The *meta* orange shift at 130.5 ppm (G) and the *ortho* green shift at 131.5 ppm (F) are close to two medium-intensity experimental peaks. Both *meta* orange shifts at 120.5 ppm (J) and 121 ppm (I) are adjacent to stronger experimental peaks. The overlap at 134.5 ppm (*ortho* green in D and *para* purple in E) is close to the experimental peak at 136 ppm. The *meta* orange shift at 127.8 ppm (H) is within less than 1 ppm from the sharpest experimental peak at 129 ppm. This good correspondence between the experimental and theoretical peaks indicates that the HCTH407/6-311+G(2d,p) level of theory seems to produce rather accurate $^{13}$C-NMR predictions for the commercial OAPS. In addition, the

same number of experimental and predicted shifts confirms that all three isomers are present in the experimental sample.

Fig. 14b shows that each predicted *meta* or *para* shift is also very close to an adjacent experimental peak in the controlled OAPS sample. The predicted B and C shifts are next to weak experimental signals at 151 ppm and 148 ppm, respectively. The same correspondence can be observed for the G, H, I, J, K and L predicted shifts with adjacent experimental signals. Two *para* shifts, E and O, correspond to the main experimental peaks at 135 ppm and 113 ppm respectively. As expected, there are only ten peaks in the experimental spectrum. This confirms the absence of the *ortho* isomer in the controlled sample, whereas there are sixteen peaks in (a) for the commercial OAPS.

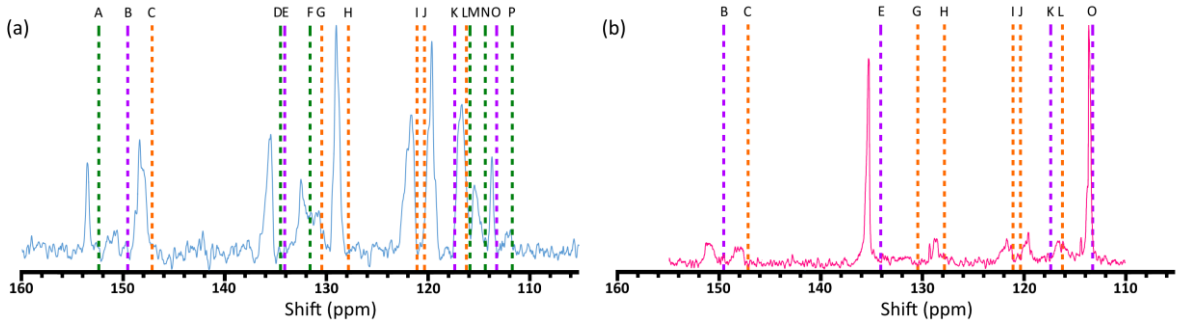


**Fig. 14.** The experimental $^{13}$C-NMR spectra of (a) the commercial OAPS (blue line) and (b) the controlled OAPS (pink line) compared to the predicted shifts from DFT calculations using Gaussian (dashed lines) at the HCTH407/6-311+G(2d,p) level of theory for the three OAPS isomers.

For the commercial sample, the MAE and RMSE are 0.80 ppm and 0.90 ppm. For the controlled sample, the MAE and RMSE are 0.80 ppm and 0.95 ppm. These RMSE values are much smaller than the values of 1.89 ppm reported by Abil et al. [43] and 4.46 ppm reported by Zhang et al. [103] for other molecules.

Fig. 15 shows the linear correlations [43] between the $\delta_{calc}$ and $\delta_{exp}$ $^{13}$C-NMR shifts for the commercial and controlled samples, respectively. The slopes are close to 1 and the correlations are very good ($R > 0.998$).

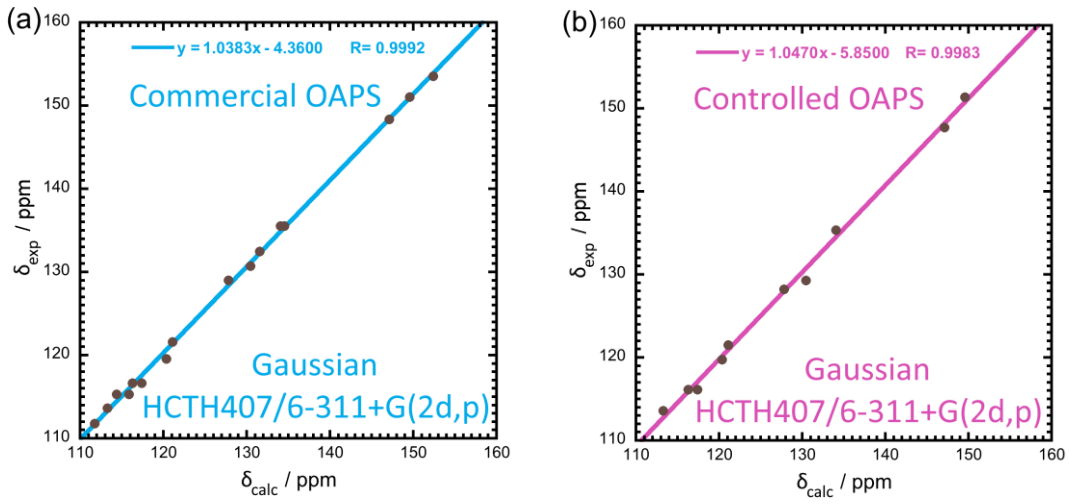


**Fig. 15.** Linear correlation between the $\delta_{calc}$, as predicted by DFT at the HCTH407/6-3+G(2d,p) level of theory, and $\delta_{exp}$ for the $^{13}$C-NMR shifts in (a) the commercial OAPS and (b) the controlled OAPS

Using the correlations shown in Fig. 15, the $\delta_{calc}$ originating from Gaussian can be scaled [43, 89, 95] using a similar approach to that of the IR wavenumbers (Section 2.2) in order for them to be even closer to the experimental $\delta_{exp}$. These scaled predicted shifts $\delta_{calc\_scaled}$ are reported in Tables 4 and 5 for the commercial and controlled OAPS, respectively. They decrease the MAE and RMSE to 0.44 ppm and 0.54 ppm for the commercial OAPS, and to 0.66 ppm and 0.75 ppm for the controlled OAPS.

**Table 4.** Comparison between the predicted scaled $\delta_{calc\_scaled}$ and experimental $\delta_{exp}$ $^{13}$C-NMR shifts in ppm along with their absolute error $|e_i|$ in ppm for each peak identified in the commercial OAPS sample (Fig. 14a).

| C Type | $\delta_{calc\_scaled}$ | $\delta_{exp}$ | $\|e_i\|$ | Identification | Isomer type |
|---|---|---|---|---|---|
| $C_1$ | 131.09 | 130.70 | 0.39 | G | meta |
| $C_2$ | 120.61 | 119.55 | 1.06 | J | meta |
| $C_3$ | 148.41 | 148.34 | 0.07 | C | meta |
| $C_4$ | 116.39 | 116.64 | 0.25 | L | meta |
| $C_5$ | 128.36 | 128.97 | 0.61 | H | meta |
| $C_6$ | 121.39 | 121.60 | 0.21 | I | meta |
| $C_1$ | 111.67 | 111.78 | 0.11 | P | ortho |
| $C_2$ | 153.89 | 153.53 | 0.36 | A | ortho |
| $C_3$ | 114.42 | 115.28 | 0.86 | N | ortho |
| $C_4$ | 132.27 | 132.45 | 0.18 | F | ortho |
| $C_5$ | 115.98 | 115.28 | 0.70 | M | ortho |
| $C_6$ | 135.32 | 135.54 | 0.22 | D | ortho |
| $C_1$ | 117.56 | 116.64 | 0.92 | K | para |
| $C_2$ | 134.87 | 135.54 | 0.67 | E | para |
| $C_3$ | 113.26 | 113.60 | 0.34 | O | para |
| $C_4$ | 150.94 | 151.00 | 0.06 | B | para |

**Table 5.** Same as Table 4 but for the controlled OAPS sample (Fig. 14b).

| C-Type | $\delta_{calc\_scaled}$ | $\delta_{exp}$ | $\lvert e_i \rvert$ | Identification | Isomer type |
|---|---|---|---|---|---|
| $C_1$ | 130.73 | 129.28 | 1.45 | G | meta |
| $C_2$ | 120.17 | 119.74 | 0.43 | J | meta |
| $C_3$ | 148.19 | 147.71 | 0.48 | C | meta |
| $C_4$ | 115.91 | 116.13 | 0.22 | L | meta |
| $C_5$ | 127.98 | 128.20 | 0.22 | H | meta |
| $C_6$ | 120.95 | 121.51 | 0.56 | I | meta |
| $C_1$ | 117.09 | 116.13 | 0.96 | K | para |
| $C_2$ | 134.54 | 135.35 | 0.81 | E | para |
| $C_3$ | 112.76 | 113.59 | 0.83 | O | para |
| $C_4$ | 150.75 | 151.36 | 0.61 | B | para |

These analyses confirm that DFT at the HCTH407/6-311+G(2d,p) level of theory is able to predict very accurately the $^{13}$C-NMR shifts for all OAPS isomers, regardless of whether there are three isomers (commercial sample) or only two isomers (controlled sample).

### 3.3.2. *The $^1$H-NMR predicted spectra for all three isomers*

The $^1$H-NMR spectra were predicted for all three isomers using both MestreNova and DFT at the HCTH407/6-311+G(2d,p) level of theory. They are compared to those of the experimental (a) commercial and (b) controlled OAPS in Fig. 16 for MestreNova and in Fig. 17 for Gaussian. The letters used to identify the predicted peaks for the aromatic hydrogens are those of their adjacent aromatic carbons (Tables 4 & 5). The amine hydrogens are referred to by the name of their isomer.

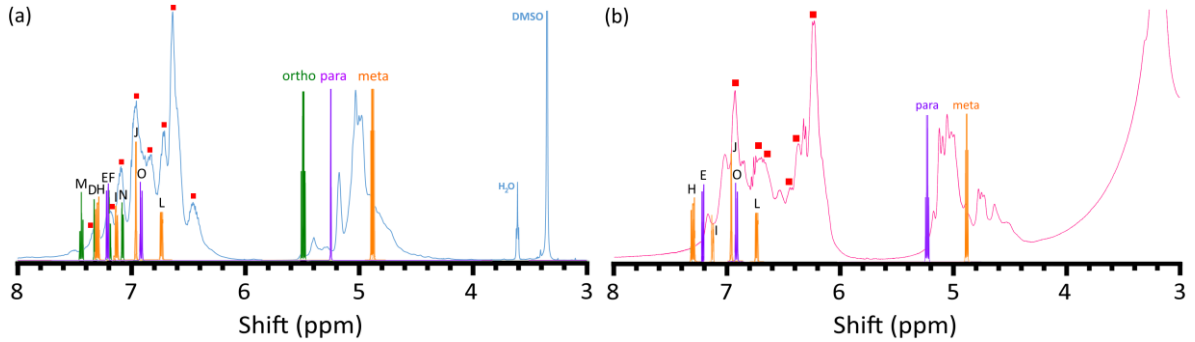


**Fig. 16.** The experimental $^{1}$H-NMR spectra of (a) the commercial OAPS (blue line) and (b) the controlled OAPS (pink line) compared with the predicted shifts by MestreNova for the three isomers.

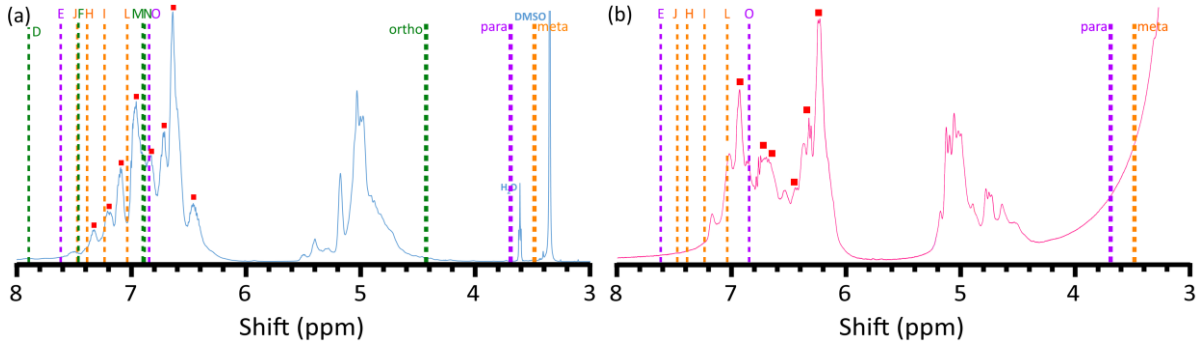


**Fig. 17.** As Fig. 16 but for the Gaussian DFT-predicted shifts at the HCTH407/6-311+G(2d,p) level of theory.

For the aromatic hydrogens of the commercial sample (left regions of Fig. 16a and Fig. 17a), ten slightly overestimated shifts are predicted by both MestreNova and Gaussian, with four of them overlapping. As a result, only eight peaks are observable from 6.7 ppm to 7.9 ppm, in agreement with the eight observable experimental shifts (red rectangles). However, the relative order of these peaks is somewhat different between MestreNova and Gaussian, which means that both codes do not assign the same peaks to the same isomer. For the amine hydrogens (right regions of Fig. 16a and Fig. 17a), three MestreNova shifts are predicted in the range 4.9-5.5 ppm, *i.e.* close to the three experimental peaks, which is compatible with the presence of all isomers. Gaussian also predicts three separate shifts albeit, as noted before, in a range from 3.5 to 4.5 ppm which is somewhat lower than the experimental values. Unlike the aromatic hydrogens, both predicted sets of amine hydrogen shifts are in the same relative order.

The situation is similar for the predicted amine hydrogen shifts in the controlled OAPS (right regions of Fig. 16b and Fig. 17b), where the experimental peak related to the *ortho* isomer disappears. For

the aromatic hydrogens (left regions of Fig. 16b and Fig. 17b), the predicted shifts are in the range above 6.6 ppm, they are again slightly displaced towards higher values compared to the experiment and their identification differs according to the method used. There are six of them, which relate to the six observable experimental shifts for the *meta* and *para* isomers (red rectangles).

The MestreNova MAE and RMSE for the $^{1}$H-NMR shifts of the commercial OAPS are 0.16 ppm and 0.18 ppm, respectively. If the amine hydrogens are removed from the calculations, the aromatic hydrogens MAE and RMSE are 0.18 ppm and 0.19 ppm. The MAE and RSME for the controlled OAPS are 0.39 ppm and 0.42 ppm when all hydrogens are taken into account, and 0.47 ppm for both when only the aromatic hydrogens are considered. The corresponding Gaussian MAE and RMSE for all hydrogens in the commercial OAPS are 0.60 ppm and 0.74 ppm, respectively. Those related to the aromatic hydrogens are 0.37 ppm and 0.38 ppm. The MAE and RMSE for the controlled OAPS are 0.85 ppm and 0.90 ppm, whereas they decrease to 0.69 and 0.70 after removing the amine shifts. The fact that the MAE and RMSE are close to each other indicates that the errors are not scattered.

Fig. 18 and Fig. 19 illustrate the linear correlations for the commercial and controlled OAPS, respectively, between the $\delta_{exp}$ and the $\delta_{calc}$ $^{1}$H-NMR shifts predicted by both MestRenova and Gaussian while only taking into account the aromatic hydrogens. This removes the problem of the amine shifts. All cases are well correlated (R > 0.97).

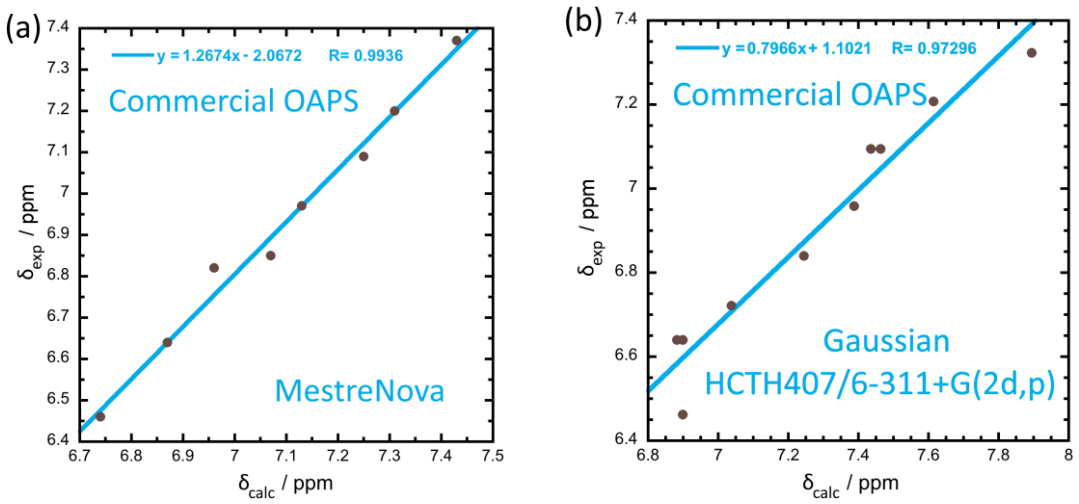


**Fig. 18**. Linear correlation between the $\delta_{calc}$ and the $\delta_{exp}$ $^{1}$H-NMR shifts predicted by (a) MestreNova and (b) DFT at the HCTH407/6-311+G(2d,p) level of theory while only taking into account the aromatic hydrogens in the commercial OAPS (Fig. 16a and Fig. 17a).

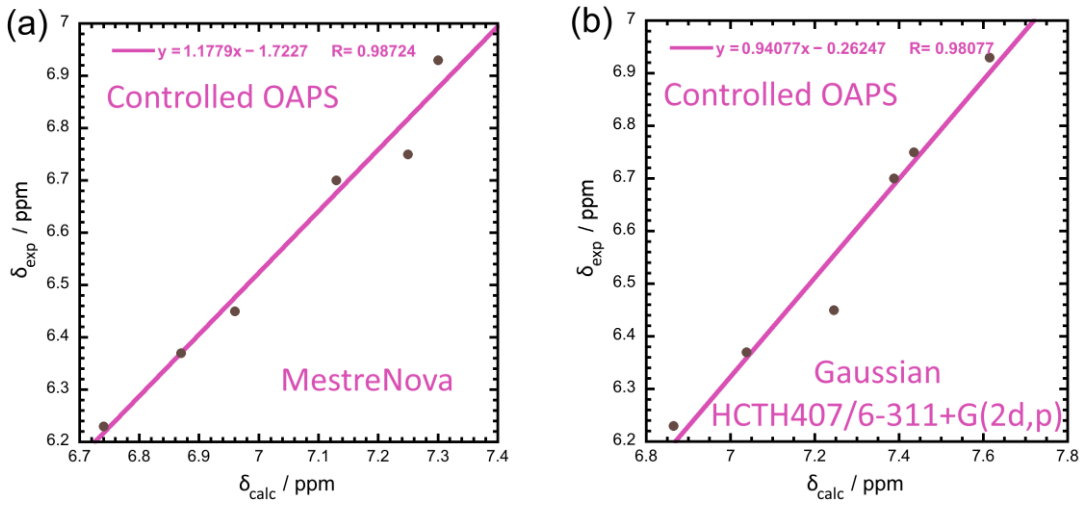


**Fig. 19.** As Fig. 18 but for the controlled OAPS (Fig. 16b and Fig. 17b).

As before, the scaled predicted shifts $\delta_{calc\_scaled}$ were obtained for both commercial and controlled OAPS from the correlations shown in Fig. 18 and Fig. 19. The MestRenova-predicted $\delta_{calc\text{-}scaled}$ for the commercial OAPS are reported in Table 6: compared to the unscaled aromatic hydrogens predictions, both MAE and RMSE fall to 0.03 ppm. The corresponding Gaussian-predicted $\delta_{calc\text{-}scaled}$ are reported in Table 7: the MAE and RMSE fall to 0.05 ppm and 0.06 ppm respectively. The MestRenova $\delta_{calc\text{-}scaled}$ for the controlled OAPS are reported in Table 8: the MAE and RMSE are reduced to 0.03 ppm and 0.04 ppm. The Gaussian-predicted $\delta_{calc\_scaled}$ shifts for the controlled OAPS are reported in Table 9: the MAE and RMSE are reduced to 0.08 ppm. Precise values for the OAPS aromatic hydrogens shifts can thus be obtained from both prediction methods when associated with the appropriate scaling.

**Table 6.** The scaled MestreNova-predicted $\delta_{calc\_scaled}$ and experimental $\delta_{exp}$ $^{1}$H-NMR shifts in ppm along with their absolute error $|e_i|$ in ppm for each hydrogen peak identified in the commercial OAPS (Fig. 16a).

| H-Type | $\delta_{calc\_scaled}$ | $\delta_{exp}$ | $\|e_i\|$ | Identification | Isomer type |
|---|---|---|---|---|---|
| $H_{C2}$ | 6.75 | 6.71 | 0.04 | J | meta |
| $H_{C4}$ | 6.48 | 6.46 | 0.02 | L | meta |
| $H_{C5}$ | 7.18 | 7.21 | 0.03 | H | meta |
| $H_{C6}$ | 6.97 | 6.95 | 0.02 | I | meta |
| $H_{C3}$ | 6.91 | 6.84 | 0.08 | N | ortho |
| $H_{C4}$ | 7.05 | 7.09 | 0.02 | F | ortho |
| $H_{C5}$ | 7.35 | 7.32 | 0.03 | M | ortho |
| $H_{C6}$ | 7.20 | 7.21 | 0.01 | D | ortho |
| $H_{C2}$ | 7.12 | 7.09 | 0.03 | E | para |
| $H_{C3}$ | 6.64 | 6.63 | 0.01 | O | para |

**Table 7.** As Table 6 but for Gaussian and the commercial OAPS (Fig. 17a).

| H-Type | $\delta_{calc\_scaled}$ | $\delta_{exp}$ | $\|e_i\|$ | Identification | Isomer type |
|---|---|---|---|---|---|
| $H_{C2}$ | 7.03 | 7.09 | 0.06 | J | meta |
| $H_{C4}$ | 6.71 | 6.72 | 0.01 | L | meta |
| $H_{C5}$ | 6.99 | 6.96 | 0.03 | H | meta |
| $H_{C6}$ | 6.87 | 6.84 | 0.03 | I | meta |
| $H_{C3}$ | 6.58 | 6.64 | 0.06 | N | ortho |
| $H_{C4}$ | 7.05 | 7.09 | 0.04 | F | ortho |
| $H_{C5}$ | 6.60 | 6.64 | 0.04 | M | ortho |
| $H_{C6}$ | 7.39 | 7.32 | 0.07 | D | ortho |
| $H_{C2}$ | 7.17 | 7.21 | 0.04 | E | para |
| $H_{C3}$ | 6.60 | 6.46 | 0.14 | O | para |

**Table 8.** As Table 6 but for MestRenova and the controlled OAPS (Fig. 16b).

| H-Type | $\delta_{calc\_scaled}$ | $\delta_{exp}$ | $\lvert e_i \rvert$ | Identification | Isomer type |
|---|---|---|---|---|---|
| $H_{C2}$ | 6.48 | 6.45 | 0.03 | J | meta |
| $H_{C4}$ | 6.22 | 6.23 | 0.01 | L | meta |
| $H_{C5}$ | 6.88 | 6.93 | 0.05 | H | meta |
| $H_{C6}$ | 6.68 | 6.7 | 0.02 | I | meta |
| $H_{C2}$ | 6.82 | 6.75 | 0.07 | E | para |
| $H_{C3}$ | 6.37 | 6.37 | 0.00 | O | para |

**Table 9.** As Table 6 but for Gaussian and the controlled OAPS (Fig. 17b).

| H-Type | $\delta_{calc\_scaled}$ | $\delta_{exp}$ | $\lvert e_i \rvert$ | Identification | Isomer type |
|---|---|---|---|---|---|
| $H_{C2}$ | 6.73 | 6.75 | 0.02 | J | meta |
| $H_{C4}$ | 6.36 | 6.37 | 0.01 | L | meta |
| $H_{C5}$ | 6.55 | 6.70 | 0.15 | H | meta |
| $H_{C6}$ | 6.69 | 6.45 | 0.24 | I | meta |
| $H_{C2}$ | 6.90 | 6.93 | 0.03 | E | para |
| $H_{C3}$ | 6.20 | 6.23 | 0.03 | O | para |

In spite of the slight displacements between predicted and experimental peaks, both MestreNova and DFT at the HCTH407/6-311+G(2d,p) level of the theory seem to be able to provide compatible results with the experimental $^{1}$H-NMR shifts for OAPS. However, it remains unclear why the relative order of the predicted aromatic hydrogens peaks differ, *i.e.* the identification of each peak as belonging to a specific isomer depends on the prediction method used. Since it was not possible to differentiate both methods for $^{1}$H-NMR using the one-dimensional NMR spectra only, it was attempted to predict the 2D-NMR $^{13}$C-NMR vs $^{1}$H-NMR spectra with each of them.

### 3.4. *2D-NMR predictions*

The $^{13}$C-NMR $\delta_{calc\_scaled}$ shifts (Section 3.2) for both types of OAPS were combined in Fig. 20 with their respective aromatic $^{1}$H-NMR $\delta_{calc\_scaled}$ shifts (Section 3.3) in order to predict 2D-NMR spectra comparable to the available experimental HSQC spectra. Fig. 20a and Fig. 20b show the predictions by

MestreNova and Gaussian, respectively, for the commercial OAPS, while Fig. 20c and Fig. 20d are the corresponding predictions for the controlled OAPS.

In the predicted 2D-NMR spectrum of the commercial OAPS with MestreNova (Fig. 20a), some peaks can easily be assigned. The G, P and K shifts on the $^{13}$C-NMR axis are related to the *meta*, *ortho*, and *para* aromatic carbons connected to the silicons in the OAPS cages. Similarly, the C, A and B shifts correspond to the carbons connected to the amine nitrogens. The other $^{13}$C-NMR shifts are associated with the aromatic hydrogens and their cross-points can be compared to the experimental spectrum. However, it is clear that the predicted cross-points are scattered and far from the experimental data (for example M and N). The situation improves significantly for the predicted 2D-NMR spectrum of the commercial OAPS with Gaussian (Fig. 20b). The G, P, K, C, A and B shifts on the $^{13}$C-NMR axis can again be assigned to the carbons linked either to the OAPS cage silicons or to the amine nitrogens. As far as the cross-points are concerned, the *ortho* D, *para* E, *ortho* F and *meta* H shifts correspond very well to experimental contour lines. The other cross-points are slightly more displaced because of the differences between predicted and experimental peaks. The largest deviation of the prediction from its corresponding counter line seems to be the *meta* L peak, which could be due to an underestimation in the $^{13}$C-NMR spectrum. However, the Gaussian-predicted cross-points still reproduce rather well the ten contour points of the experimental HSQC spectrum, i.e. the prediction is much better than that of MestreNova in Fig. 20a.

In the predicted 2D-NMR spectrum of the controlled OAPS with MestreNova (Fig. 20c), the G, K, B and C shifts on the $^{13}$C-NMR axis are related to the carbons connected either to the cage silicons or to the amine nitrogens. For the carbons connected to aromatic hydrogens, the black rectangles suggest that the two sharpest $^{13}$C-NMR peaks, which correspond to large contour cross-points, can be assigned to the *para* isomer. On the other hand, the H, I, J and L shifts can be assigned to the *meta* isomer. However, as for (a), the predicted shifts for the aromatic hydrogens lead to cross-points that are displaced with respect to the experimental signals, even if there is a better agreement than for the commercial OAPS. The situation for the predicted 2D-NMR spectrum of the controlled OAPS improves once again with Gaussian (Fig. 20d). The assignment of each peak to a specific isomer is similar to MestreNova but the cross-points are much closer to the experimental adjacent contour point. The black rectangles confirm that the sharp $^{13}$C-NMR peaks correspond to the *para* isomer.

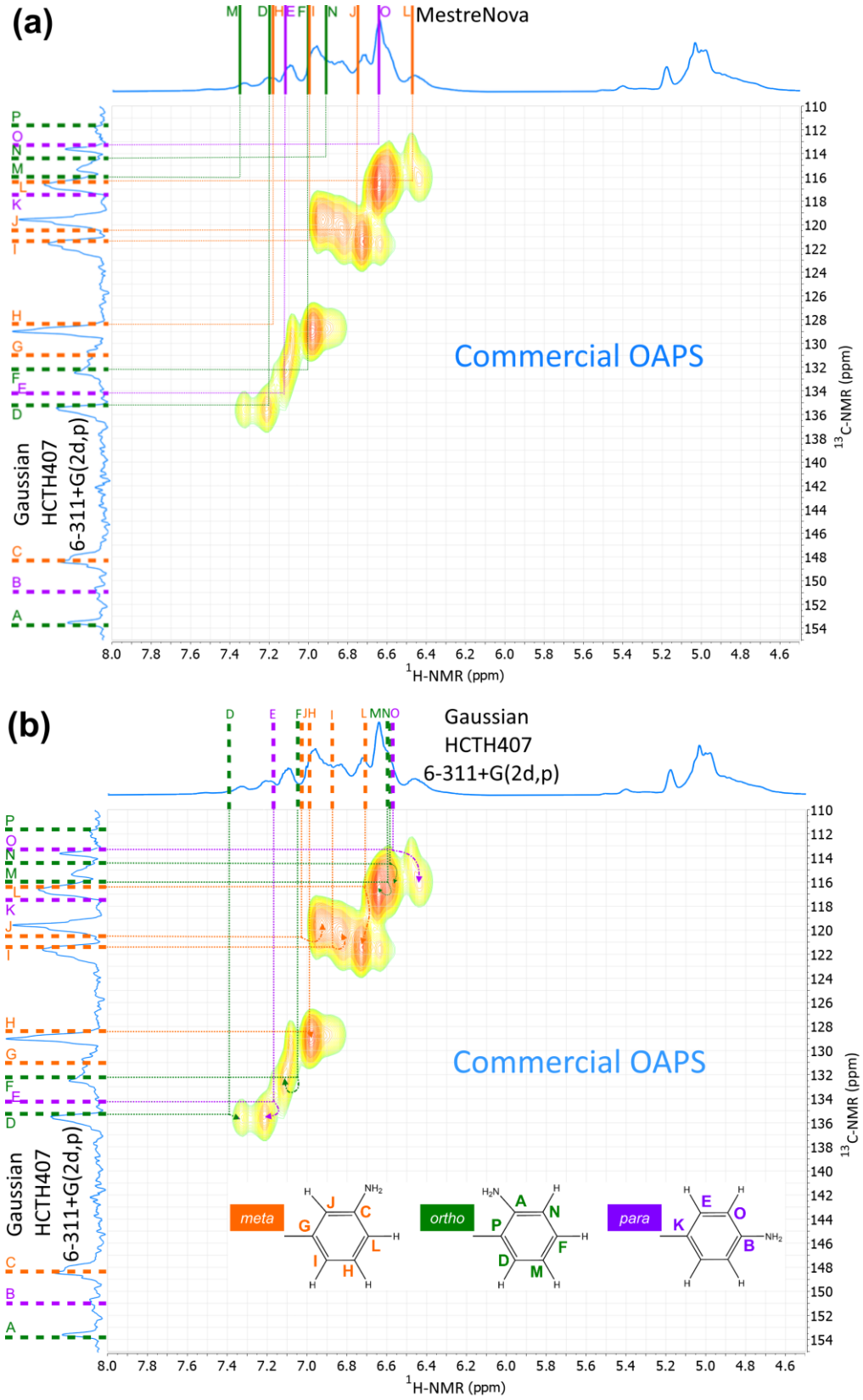
(a)
MestreNova
Commercial OAPS
Gaussian
HCTH407
6-311+G(2d,p)
$^{1}$H-NMR (ppm)
$^{13}$C-NMR (ppm)
(b)
Gaussian
HCTH407
6-311+G(2d,p)
Commercial OAPS
meta
ortho
para
$^{1}$H-NMR (ppm)
$^{13}$C-NMR (ppm)

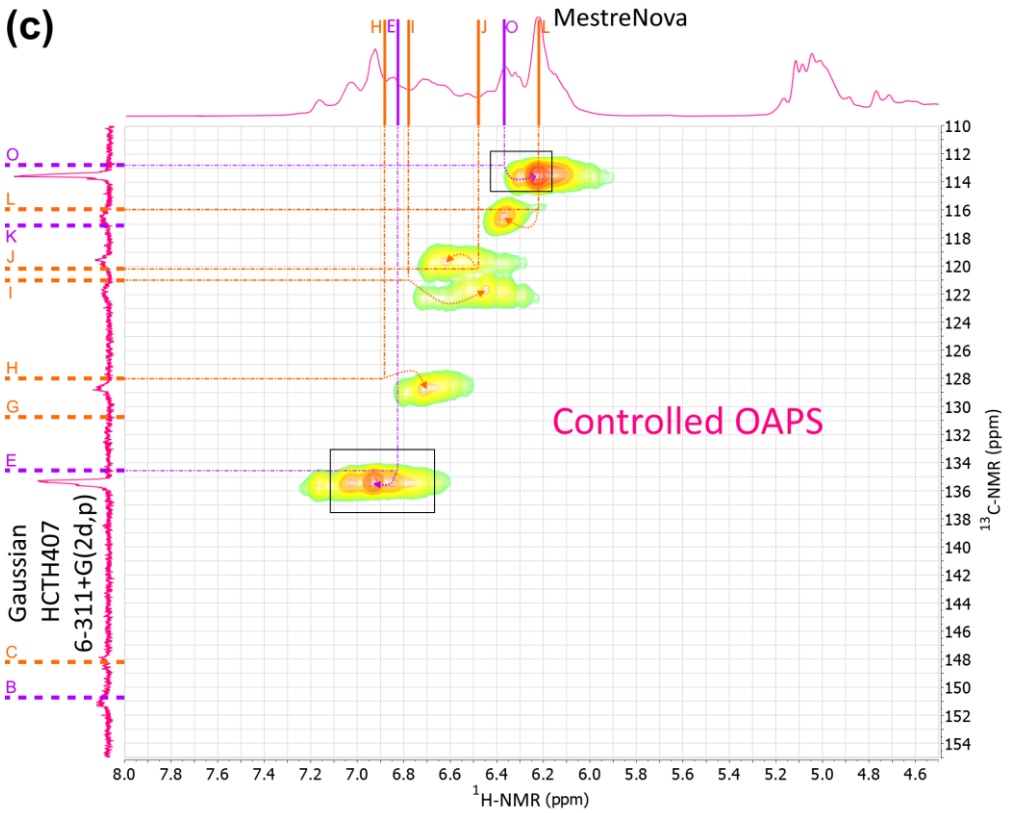
(c)
MestreNova
H E I J O L
O L K J I H G E C B
Gaussian HCTH407 6-311+G(2d,p)
Controlled OAPS
110 112 114 116 118 120 122 124 126 128 130 132 134 136 138 140 142 144 146 148 150 152 154
13C-NMR (ppm)
8.0 7.8 7.6 7.4 7.2 7.0 6.8 6.6 6.4 6.2 6.0 5.8 5.6 5.4 5.2 5.0 4.8 4.6
1H-NMR (ppm)

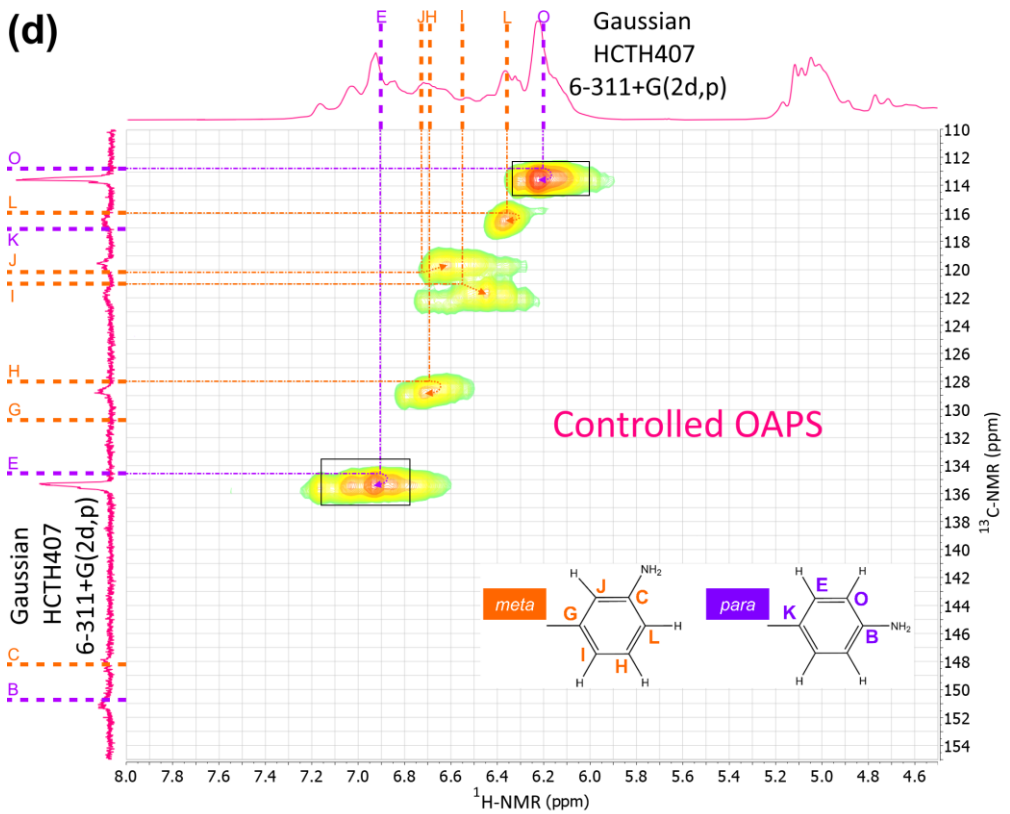
(d)
E J H I L O
Gaussian HCTH407 6-311+G(2d,p)
O L K J I H G E C B
Gaussian HCTH407 6-311+G(2d,p)
Controlled OAPS
meta
para
110 112 114 116 118 120 122 124 126 128 130 132 134 136 138 140 142 144 146 148 150 152 154
13C-NMR (ppm)
8.0 7.8 7.6 7.4 7.2 7.0 6.8 6.6 6.4 6.2 6.0 5.8 5.6 5.4 5.2 5.0 4.8 4.6
1H-NMR (ppm)

**Fig. 20**. The experimental HSQC spectrum for the commercial (blue) and controlled (pink) OAPS compared to the $\delta_{calc\_scaled}$ for the $^{13}$C-NMR shifts (*y*-axis) predicted by Gaussian at the HCTH407/6-311+G(2d,p) level of theory (a-d), and compared to the $^{1}$H-NMR shifts (*x*-axis) predicted by MestreNova (a & c), and Gaussian at the same level of theory (b & d). The colours for the isomers are orange for *meta*, green for *ortho* and purple for *para*.

While it was difficult to unambiguously assess the quality of the MestreNova and Gaussian predictions for $^{1}$H-NMR using the one-dimensional spectra only, the 2D-NMR predictions prove that the Gaussian calculations with DFT are much better at predicting accurate chemical shifts for $^{1}$H-NMR than MestreNova.

Consequently, the final isomer assignment for each peak is that predicted by Gaussian with DFT at the HCTH407/6-311+G(2d,p) level of theory. It is summarized in Table 10.

**Table 10.** The Gaussian-predicted $\delta_{calc\_scaled}$ compared to the $\delta_{exp}$ for the $^{13}$C-NMR and $^{1}$H-NMR chemical shifts in ppm for each aromatic carbon and hydrogen peak identified in the commercial and controlled OAPS samples and the assignment of each signal to a specific isomer (Tables 4-9).

| H and C Type | Commercial $\delta_{calc\_scaled}$ | Commercial $\delta_{exp}$ | Controlled $\delta_{calc\_scaled}$ | Controlled $\delta_{exp}$ | Identification | Isomer type |
|---|---|---|---|---|---|---|
| $C_1$ | 131.09 | 130.70 | 130.73 | 129.28 | G | meta |
| $H_{C2}$ - $C_2$ | 7.03-120.61 | 7.09-119.55 | 6.73-120.17 | 6.75-119.74 | J | meta |
| $C_3$ | 148.41 | 148.34 | 148.19 | 147.71 | C | meta |
| $H_{C4}$ - $C_4$ | 6.71-116.39 | 6.72-116.64 | 6.36-115.91 | 6.37-116.13 | L | meta |
| $H_{C5}$ - $C_5$ | 6.99-128.36 | 6.96-128.97 | 6.55-127.98 | 6.70-128.20 | H | meta |
| $H_{C6}$ - $C_6$ | 6.87-121.39 | 6.84-121.60 | 6.69-120.95 | 6.45-121.51 | I | meta |
| $C_1$ | 111.67 | 111.78 | - | - | P | ortho |
| $C_2$ | 153.89 | 153.53 | - | - | A | ortho |
| $H_{C3}$ - $C_3$ | 6.58-114.42 | 6.64-115.28 | - | - | N | ortho |
| $H_{C4}$ - $C_4$ | 7.05-132.27 | 7.09-132.45 | - | - | F | ortho |
| $H_{C5}$ - $C_5$ | 6.60-115.98 | 6.64-115.28 | - | - | M | ortho |
| $H_{C6}$ - $C_6$ | 7.39-135.32 | 7.32-135.54 | - | - | D | ortho |
| $C_1$ | 117.56 | 116.64 | 117.09 | 116.13 | K | para |
| $H_{C2}$ - $C_2$ | 7.17-134.87 | 7.21-135.54 | 6.90-134.54 | 6.93-135.35 | E | para |
| $H_{C3}$ - $C_3$ | 6.60-113.26 | 6.46-113.60 | 6.20-112.76 | 6.23-113.59 | O | para |
| $C_4$ | 150.94 | 151.00 | 150.75 | 151.36 | B | para |

# Conclusions

Experimental characterizations were carried out both for a commercial OAPS containing all three isomers and for a controlled OAPS containing only the *para* and *meta* isomers. This included pycnometry, which showed that the densities of the commercial and controlled OAPS samples were close, i.e. respectively 1.39±0.01 g/cm$^3$ and 1.37±0.01 g/cm$^3$. Density thus seems rather insensitive to the nature and the proportions of the isomers. On the other hand, the IR, as well as the $^{13}$C-NMR and the $^{1}$H-

NMR spectra in one dimension and two dimensions were found to be more isomer-specific. To better identify the isomers, the experimental results were compared to predictions of the IR and NMR spectra from DFT quantum mechanical methods and machine-learning techniques.

IR predictions allowed for the identification of the various modes of vibrations and assigned some of the experimental peaks to specific isomers. The one-dimensional and two-dimensional NMR predictions were more difficult to carry out as the results were dependent on the method and the level of theory used. The Gaussian DFT-predicted shifts at the HCTH407/6-311+(2d,p) level of theory were found to be consistent with the experimental $^{13}$C-NMR and $^{1}$H-NMR shifts. MestreNova was also tested for the prediction of the $^{1}$H-NMR shifts but did not give accurate results when compared with the 2-D HSQC OAPS experimental spectra. On the other hand, the Gaussian DFT-predicted shifts were found, when scaled, to correspond well to the contour clouds of the 2-D NMR spectra for both the commercial OAPS (3 isomers) and the controlled OAPS (2 isomers) samples. Within this context, quantum mechanical methods are clearly superior to machine-learning methods, despite being computationally much more expensive. As a result, each peak in the $^{13}$C-NMR and $^{1}$H-NMR OAPS spectra could be assigned to a specific isomer using the Gaussian DFT-predictions.

# Acknowledgements

This work is part of the MOLHYB project financed by the French ANR (*Agence Nationale de la Recherche*) within the framework of the AAPG (*Appel à Projets Générique*) 2018. This work had access to the HPC resources of CCRT/CINES/IDRIS under the allocations A009- and A011-095053 made by GENCI, France. The MUST computing centre at the University Savoie Mont Blanc, France, is also acknowledged for the provision of computer time. Nicolas Charvin is thanked for his help with the installation and maintenance of the laboratory local servers.

# References


[1] D.B. Cordes, P.D. Lickiss, F. Rataboul, Recent developments in the chemistry of cubic polyhedral oligosilsesquioxanes, Chemical Reviews 110(4) (2010) 2081-2173, doi:10.1021/cr900201r.

[2] A.F. Hill, M.J. Fink, Advances in Organometallic Chemistry, Academic Press2008.

[3] H. Rios-Dominguez, F. Ruiz-Trevino, R. Contreras-Reyes, A. Gonzalez-Montiel, Syntheses and evaluation of gas transport properties in polystyrene–POSS membranes, Journal of Membrane Science 271(1-2) (2006) 94-100, doi:10.1016/j.memsci.2005.07.014.

[4] B.S. Reddy, D. Gnanasekaran, Structure-gas transport property relationships of poly (dimethylsiloxane-urethane) nanocomposite membranes, Advances in Nanocomposites–Synthesis, Characterization and Industrial Applications, Intech–Publishing Croatia2011, pp. 195-226.

[5] R. Tamaki, Y. Tanaka, M.Z. Asuncion, J. Choi, R.M. Laine, Octa (aminophenyl) silsesquioxane as a nanoconstruction site, Journal of the American Chemical Society 123(49) (2001) 12416-12417, doi:10.1021/ja011781m.

[6] Gelest Inc. https://www.gelest.com/. (Accessed 11th March 2022).

[7] P. Iyer, G. Iyer, M. Coleman, Gas transport properties of polyimide–POSS nanocomposites, Journal of Membrane Science 358(1-2) (2010) 26-32, doi:10.1016/j.memsci.2010.04.023.

[8] W.R. Kang, A.S. Lee, S. Park, S.-H. Park, K.-Y. Baek, K.B. Lee, S.-H. Lee, J.-H. Lee, S.S. Hwang, J.S. Lee, Free-standing, polysilsesquioxane-based inorganic/organic hybrid membranes for gas separations, Journal of Membrane Science 475 (2015) 384-394, doi:10.1016/j.memsci.2014.10.024.

[9] Y. Kinoshita, K. Wakimoto, A.H. Gibbons, A.P. Isfahani, H. Kusuda, E. Sivaniah, B. Ghalei, Enhanced PIM-1 membrane gas separation selectivity through efficient dispersion of functionalized POSS fillers, Journal of Membrane Science 539 (2017) 178-186, doi:10.1016/j.memsci.2017.05.072.

[10] S. Neyertz, D. Brown, S. Salimi, F. Radmanesh, N.E. Benes, Molecular characterization of polyOAPS-imide isomer hyper-cross-linked membranes: Free-volume morphologies and sorption isotherms for $CH_4$ and $CO_2$, Journal of Membrane Science (2021) 119531, doi:10.1016/j.memsci.2021.119531.

[11] S. Neyertz, S. Salimi, F. Radmanesh, N.E. Benes, D. Brown, High-temperature molecular screening of hybrid polyOAPS-imide networks based on octa (aminophenyl) silsesquioxane for increased thermomechanical resistance, Physical Chemistry Chemical Physics 23(19) (2021) 11438-11454, doi:10.1039/D1CP01052B.

[12] J. Choi, R. Tamaki, S.G. Kim, R.M. Laine, Organic/inorganic imide nanocomposites from aminophenylsilsesquioxanes, Chemistry of Materials 15(17) (2003) 3365-3375, doi:10.1021/cm030286h.

[13] R. Tamaki, J. Choi, R.M. Laine, A polyimide nanocomposite from octa (aminophenyl) silsesquioxane, Chemistry of Materials 15(3) (2003) 793-797, doi:10.1021/cm020797o.

[14] S. Kim, J. Choi, R. Tamaki, R.M. Laine, Synthesis of amino-containing oligophenylsilsesquioxanes, Polymer 46(12) (2005) 4514-4524, doi:10.1016/j.polymer.2005.02.036.

[15] K. Takahashi, S. Sulaiman, J.M. Katzenstein, S. Snoblen, R.M. Laine, New Aminophenylsilsesquioxanes—Synthesis, Properties, and Epoxy Nanocomposites, Australian Journal of Chemistry 59(8) (2006) 564-570, doi:10.1071/CH06153.

[16] M.Z. Asuncion, R.M. Laine, Silsesquioxane barrier materials, Macromolecules 40(3) (2007) 555-562, doi:10.1021/ma062305p.

[17] R.M. Laine, M.F. Roll, Polyhedral phenylsilsesquioxanes, Macromolecules 44(5) (2011) 1073-1109, doi:10.1021/ma102360t.

[18] J. Choi, S.G. Kim, R.M. Laine, Organic/inorganic hybrid epoxy nanocomposites from aminophenylsilsesquioxanes, Macromolecules 37(1) (2004) 99-109, doi:10.1021/ma030309d.

[19] S. Sulaiman, Synthesis and characterization of polyfunctional Polyhedral Silsesquioxane Cages, University of Michigan, 2011.

[20] A. Lee, T.S. Haddad, J.J. Schwab, Y.Z. An, Molecular Structure Analysis of Aminophenyl Silsesquioxane, Michigan State Univ., 2006.

[21] MestreNova, Mestrelab Research. https://mestrelab.com/. (Accessed 11th March 2022).

[22] M.J. Frisch, G.W. Trucks, H.B. Schlegel, G.E. Scuseria, M.A. Robb, J.R. Cheeseman, G. Scalmani, V. Barone, B. Mennucci, G.A. Petersson, H. Nakatsuji, M. Caricato, X. Li, H.P. Hratchian, A.F. Izmaylov, J. Bloino, G. Zheng, J.L. Sonnenberg, M. Hada, M. Ehara, K. Toyota, R. Fukuda, J. Hasegawa, M. Ishida, T. Nakajima, Y. Honda, O. Kitao, H. Nakai, T. Vreven, J.A. Montgomery Jr., J.E. Peralta, F. Ogliaro, M. Bearpark, J.J. Heyd, E. Brothers, K.N. Kudin, V.N. Staroverov, R. Kobayashi, J. Normand, K. Raghavachari, A. Rendell, J.C. Burant, S.S. Iyengar, J. Tomasi, M. Cossi, N. Rega, J.M. Millam, M. Klene, J.E. Knox, J.B. Cross, V. Bakken, C. Adamo, J. Jaramillo, R. Gomperts, R.E. Stratmann, O. Yazyev, A.J. Austin, R. Cammi, C. Pomelli, J.W. Ochterski, R.L. Martin, K. Morokuma, V.G. Zakrzewski, G.A. Voth, P. Salvador, J.J. Dannenberg, S. Dapprich, A.D. Daniels, O. Farkas, J.B. Foresman, J.V. Ortiz, J. Cioslowski, D.J. Fox, Gaussian 09, Revision A.02, Gaussian Inc., Wallingford CT, 2009.

[23] AccuPyc II 1340, by Micromeritics Instrument Corp. https://www.micromeritics.com/Product-Showcase/AccuPyc-II-1340.aspx. (Accessed 11th March 2022).

[24] W. Bremser, HOSE—a novel substructure code, Analytica Chimica Acta 103(4) (1978) 355-365, doi:10.1016/S0003-2670(01)83100-7.

[25] A.J. Abkowicz-Bieńko, Z. Latajka, D.C. Bieńko, D. Michalska, Theoretical infrared spectrum and revised assignment for para-nitrophenol. Density functional theory studies, Chemical Physics 250(2) (1999) 123-129, doi:10.1016/S0301-0104(99)00296-7.

[26] A. Kovacs, V. Izvekov, G. Keresztury, G. Pongor, Vibrational analysis of 2-nitrophenol. A joint FT-IR, FT-Raman and scaled quantum mechanical study, Chemical Physics 238(2) (1998) 231-243, doi:10.1016/S0301-0104(98)00307-3.

[27] M.A. Palafox, DFT computations on vibrational spectra: Scaling procedures to improve the wavenumbers, Physical Sciences Reviews 3(6) (2018) 20170184, doi:10.1515/psr-2017-0184.

[28] R. Arulraj, S. Sivakumar, S. Suresh, K. Anitha, Synthesis, vibrational spectra, DFT calculations, Hirshfeld surface analysis and molecular docking study of 3-chloro-3-methyl-2, 6-diphenylpiperidin-4-one, Spectrochimica Acta Part A: Molecular and Biomolecular Spectroscopy 232 (2020) 118166, doi:10.1016/j.saa.2020.118166.

[29] O. Christiansen, Vibrational structure theory: new vibrational wave function methods for calculation of anharmonic vibrational energies and vibrational contributions to molecular properties, Physical Chemistry Chemical Physics 9(23) (2007) 2942-2953, doi:10.1039/B618764A.

[30] Y. Rippers, QM MM calculations on the membrane bound hydrogenase from Ralstonia eutropha, Technische Universität Berlin, 2015.

[31] Y.B. Band, Y. Avishai, 15 - Density Functional Theory, in: Y.B. Band, Y. Avishai (Eds.), Quantum Mechanics with Applications to Nanotechnology and Information Science, Academic Press, Amsterdam, 2013, pp. 871-889.

[32] F. Jensen, Basis set convergence of nuclear magnetic shielding constants calculated by density functional methods, Journal of chemical theory and computation 4(5) (2008) 719-727, doi:10.1021/ct800013z.

[33] M. Ibrahim, E. Koglin, Vibrational spectroscopic study of acetate group, Acta Chimica Slovenica 51(3) (2004) 453-460.

[34] M. Ibrahim, E. Koglin, Spectroscopic study of polyaniline emeraldine base: modelling approach, Acta Chimica Slovenica 52(2) (2005) 159-63.

[35] C.L. Schaffer, K.T. Thomson, Density functional theory investigation into structure and reactivity of prenucleation silica species, The Journal of Physical Chemistry C 112(33) (2008) 12653-12662, doi:10.1021/jp066534p.

[36] H.B. Hassan, Density Function Theory B3LYP/6-31G** Calculation of Geometry Optimization and Energies of Donor-Bridge-Acceptor Molecular System, Int. J. Curr. Eng. Sci. Res. 4 (2014) 2342-2345.

[37] M.D. Wodrich, C. Corminboeuf, P. von Ragué Schleyer, Systematic errors in computed alkane energies using B3LYP and other popular DFT functionals, Organic Letters 8(17) (2006) 3631-3634, doi:10.1021/ol061016i.

[38] M.D. Hanwell, D.E. Curtis, D.C. Lonie, T. Vandermeersch, E. Zurek, G.R. Hutchison, Avogadro: an advanced semantic chemical editor, visualization, and analysis platform, Journal of Cheminformatics 4(1) (2012) 17, doi:10.1186/1758-2946-4-17.

[39] Avogadro: an open-source molecular builder and visualization tool. Version 1.20. http://avogadro.cc/. (Accessed 11th March 2022).

[40] N. Öztürk, T. Özdemir, Y.B. Alpaslan, H. Gokce, G. Alpaslan, Experimental (FT-IR, Raman and NMR) and theoretical (B3LYP, B3PW91, M06-2X and CAM-B3LYP) analyses of p-tert-butylphenyl salicylate, Bilge International Journal of Science and Technology Research 2(1) (2018) 56-73, doi:10.30516/bilgesci.354763.

[41] F.L.P. Costa, A.C.F. de Albuquerque, F.M. dos Santos Jr, M.B. de Amorim, GIAO - HDFT scaling factor for $^{13}C$ NMR chemical shifts calculation, Journal of Physical Organic Chemistry 23(10) (2010) 972-977, doi:10.1002/poc.1749.

[42] V.A. Du, G.N. Stipicic, U. Schubert, $^{29}Si$ NMR Shielding Calculations Employing Density Functional Theory, Focussing on Hypervalent Silicon Compounds, European Journal of Inorganic Chemistry 2011(22) (2011) 3365-3373, doi:10.1002/ejic.201100286.

[43] A.E. Aliev, D. Courtier-Murias, S. Zhou, Scaling factors for carbon NMR chemical shifts obtained from DFT B3LYP calculations, Journal of Molecular Structure: THEOCHEM 893(1-3) (2009) 1-5, doi:10.1016/j.theochem.2008.09.021.

[44] F. Blanco, I. Alkorta, J. Elguero, Statistical analysis of $^{13}C$ and $^{15}N$ NMR chemical shifts from GIAO/B3LYP/6-311++G** calculated absolute shieldings, Magnetic Resonance in Chemistry 45(9) (2007) 797-800, doi:10.1002/mrc.2053.

[45] D. Xin, C.A. Sader, O. Chaudhary, P.-J. Jones, K. Wagner, C.S. Tautermann, Z. Yang, C.A. Busacca, R.A. Saraceno, K.R. Fandrick, Development of a $^{13}C$ NMR chemical shift prediction procedure using B3LYP/cc-pVDZ and empirically derived systematic error correction terms: a computational small molecule structure elucidation method, The Journal of Organic Chemistry 82(10) (2017) 5135-5145, doi:10.1021/acs.joc.7b00321.

[46] M. Khajehzadeh, M. Moghadam, Molecular structure, FT IR, NMR, UV, NBO and HOMO–LUMO of 1-(3-(dimethylamino) propyl)-1-(4-fluorophenyl)-1, 3-dihydroisobenzofuran-5-carbonitrile by DFT/B3LYP and PBEPBE methods with LanL2DZ and 6-311++ G (d,2p) basis sets, Spectrochimica Acta Part A: Molecular and Biomolecular Spectroscopy 180 (2017) 51-66, doi:10.1016/j.saa.2017.02.055.

[47] R. Zieliński, H. Szymusiak, Application of DFT B3LYP/GIAO and B3LYP/CSGT methods for inter-pretation of NMR spectra of flavonoids, Pol. J. Food Nutr. Sci 12 (2003) 157-162.

[48] G. Świderski, M. Kalinowska, R. Świsłocka, S. Wojtulewski, W. Lewandowski, Spectroscopic (FT-IR, FT-Raman and $^{1}H$ and $^{13}C$ NMR) and theoretical in MP2/6-311++G(d,p) and B3LYP/6-311++G(d,p) levels study of benzenesulfonic acid and alkali metal benzenesulfonates, Spectrochimica Acta Part A: Molecular and Biomolecular Spectroscopy 100 (2013) 41-50, doi:10.1016/j.saa.2012.02.047.

[49] E. Virtanen, A. Valkonen, J. Tamminen, E. Kolehmainen, Comparison of calculated DFT/B3LYP and experimental $^{13}C$ and $^{17}O$ NMR chemical shifts, *ab initio* HF/6-31G* optimised structures, and single crystal X-ray structures of some substituted methyl 5β-cholan-24-oates, Journal of Molecular Structure 650(1-3) (2003) 201-212, doi:10.1016/S0022-2860(03)00156-X.

[50] E. Virtanen, M. Nissinen, R. Suontamo, J. Tamminen, E. Kolehmainen, Comparison of epimeric methyl lithocholate and methyl iso-lithocholate molecules: single crystal X-ray structure of methyl lithocholate, *ab initio* HF/6-31G* optimized structures and experimental and calculated DFT/B3LYP $^{13}C$ NMR chemical shifts, Journal of Molecular Structure 649(3) (2003) 207-218, doi:10.1016/S0022-2860(02)00476-3.

[51] C. Zhang, P. Patschinski, D.S. Stephenson, R. Panisch, J.H. Wender, M.C. Holthausen, H. Zipse, The calculation of $^{29}Si$ NMR chemical shifts of tetracoordinated silicon compounds in the gas phase and in solution, Physical Chemistry Chemical Physics 16(31) (2014) 16642-16650, doi:10.1039/C4CP01736F.

[52] L.B. Krivdin, Computational protocols for calculating $^{13}C$ NMR chemical shifts, Progress in Nuclear Magnetic Resonance Spectroscopy 112 (2019) 103-156, doi:10.1016/j.pnmrs.2019.05.004.

[53] R. AA, A. Godarzian, $^{29}Si$ NMR chemical shift calculation for silicate species by Gaussian software, Journal of the Physical Society of Japan 74(5) (2005) 1609-1620, doi:10.1143/jpsj.74.1609.

[54] D. Avcı, S. Bahçeli, Ö. Tamer, Y. Atalay, Comparative study of DFT/B3LYP, B3PW91, and HSEH1PBE methods applied to molecular structures and spectroscopic and electronic properties of flufenpyr and amipizone, Canadian Journal of Chemistry 93(10) (2015) 1147-1156, doi:10.1139/cjc-2015-0176.

[55] J.P. Perdew, P. Ziesche, H. Eschrig, Electronic structure of solids' 91, Akademie Verlag, Berlin1991.

[56] F.A. Hamprecht, A.J. Cohen, D.J. Tozer, N.C. Handy, Development and assessment of new exchange-correlation functionals, The Journal of Chemical Physics 109(15) (1998) 6264-6271, doi:10.1063/1.477267.

[57] M. Karni, Y. Apeloig, N. Takagi, S. Nagase, *Ab Initio* and DFT Study of the $^{29}Si$ NMR Chemical Shifts in RSi⁝ SiR, Organometallics 24(26) (2005) 6319-6330, doi:10.1021/om058033g.

[58] A.D. Boese, A. Chandra, J.M. Martin, D. Marx, From *ab initio* quantum chemistry to molecular dynamics: The delicate case of hydrogen bonding in ammonia, The Journal of Chemical Physics 119(12) (2003) 5965-5980, doi:10.1063/1.1599338.

[59] M.G. Teixeira, E.S. Alvarenga, Characterization of novel isobenzofuranones by DFT calculations and 2D NMR analysis, Magnetic Resonance in Chemistry 54(8) (2016) 623-631, doi:10.1002/mrc.4411.

[60] M.V. De Almeida, M.R.C. Couri, J.V. De Assis, C.P. Anconi, H.F. Dos Santos, W.B. De Almeida, $^{1}H$ NMR analysis of O‐methyl‐inositol isomers: a joint experimental and theoretical study, Magnetic Resonance in Chemistry 50(9) (2012) 608-614, doi:10.1002/mrc.3848.

[61] D. Bashford, SCRF: Self-Consistent Reaction Field, 2011. https://www.scm.com/doc/ADF/Input/SCRF.html. (Accessed 11th March 2022).

[62] B. Mennucci, E. Cances, J. Tomasi, Evaluation of solvent effects in isotropic and anisotropic dielectrics and in ionic solutions with a unified integral equation method: theoretical bases, computational implementation, and numerical applications, The Journal of Physical Chemistry B 101(49) (1997) 10506-10517, doi:10.1021/jp971959k.

[63] S. Miertuš, J. Tomasi, Approximate evaluations of the electrostatic free energy and internal energy changes in solution processes, Chemical Physics 65(2) (1982) 239-245, doi:10.1016/0301-0104(82)85072-6.

[64] S. Miertuš, E. Scrocco, J. Tomasi, Electrostatic interaction of a solute with a continuum. A direct utilization of *ab initio* molecular potentials for the prevision of solvent effects, Chemical Physics 55(1) (1981) 117-129, doi:10.1016/0301-0104(81)85090-2.

[65] J.-L. Pascual‐ahuir, E. Silla, I. Tunon, GEPOL: An improved description of molecular surfaces. III. A new algorithm for the computation of a solvent‐excluding surface, Journal of Computational Chemistry 15(10) (1994) 1127-1138, doi:10.1002/jcc.540151009.

[66] B. Mennucci, J. Tomasi, Continuum solvation models: A new approach to the problem of solute's charge distribution and cavity boundaries, The Journal of Chemical Physics 106(12) (1997) 5151-5158, doi:10.1063/1.473558.

[67] M. Cossi, V. Barone, R. Cammi, J. Tomasi, *Ab initio* study of solvated molecules: a new implementation of the polarizable continuum model, Chemical Physics Letters 255(4-6) (1996) 327-335, doi:10.1016/0009-2614(96)00349-1.

[68] V. Barone, M. Cossi, J. Tomasi, A new definition of cavities for the computation of solvation free energies by the polarizable continuum model, The Journal of Chemical Physics 107(8) (1997) 3210-3221, doi:10.1063/1.474671.

[69] E. Cances, B. Mennucci, J. Tomasi, A new integral equation formalism for the polarizable continuum model: Theoretical background and applications to isotropic and anisotropic dielectrics, The Journal of Chemical Physics 107(8) (1997) 3032-3041, doi:10.1063/1.474659.

[70] F. Lipparini, G. Scalmani, B. Mennucci, E. Cancès, M. Caricato, M.J. Frisch, A variational formulation of the polarizable continuum model, The Journal of Chemical Physics 133(1) (2010) 014106, doi:10.1063/1.3454683.

[71] M. Caricato, Absorption and emission spectra of solvated molecules with the EOM–CCSD–PCM method, Journal of Chemical Theory and Computation 8(11) (2012) 4494-4502, doi:10.1021/ct3006997.

[72] R. Cammi, Coupled‐cluster theories for the polarizable continuum model. II. Analytical gradients for excited states of molecular solutes by the equation of motion coupled‐cluster method, International Journal of Quantum Chemistry 110(15) (2010) 3040-3052, doi:10.1002/qua.22884.

[73] G. Scalmani, M.J. Frisch, Continuous surface charge polarizable continuum models of solvation. I. General formalism, The Journal of Chemical Physics 132(11) (2010) 114110, doi:10.1063/1.3359469.

[74] J. Tomasi, B. Mennucci, E. Cances, The IEF version of the PCM solvation method: an overview of a new method addressed to study molecular solutes at the QM *ab initio* level, Journal of Molecular Structure: THEOCHEM 464(1-3) (1999) 211-226, doi:10.1016/S0166-1280(98)00553-3.

[75] R.J. Abraham, M. Mobli, Modelling $^{1}$H NMR spectra of organic compounds: theory, applications and NMR prediction software, John Wiley & Sons2008.

[76] Hyperchem(TM), Hyperchem Inc. http://www.hypercubeusa.com/. (Accessed 11th March 2022).

[77] M. Alcolea Palafox, V. Rastogi, L. Mittal, Benzonitriles: Survey of their importance and scaling of their vibrational frequencies, International journal of quantum chemistry 94(4) (2003) 189-204, doi:10.1002/qua.10561.

[78] T. Chai, R.R. Draxler, Root mean square error (RMSE) or mean absolute error (MAE)? – Arguments against avoiding RMSE in the literature, Geosci. Model Dev. 7(3) (2014) 1247-1250, doi:10.5194/gmd-7-1247-2014.

[79] M. Castellá-Ventura, E. Kassab, Comparative semiempirical and *ab initio* study of the harmonic vibrational frequencies of aniline—I. The ground state, Spectrochimica Acta Part A: Molecular Spectroscopy 50(1) (1994) 69-86, doi:10.1016/0584-8539(94)80116-9.

[80] A.G. Iriarte, E.H. Cutin, C.O. Della Védova, Infrared and Raman spectra of 2-chloro-2, 2-difluoroacetamide ($ClF_2CC(O)NH_2$), Journal of Molecular Structure 800(1-3) (2006) 154-157, doi:10.1016/j.molstruc.2006.04.009.

[81] S. Gundersen, S. Samdal, R. Seip, D.J. Shorokhov, T.G. Strand, The molecular structure, conformation, potential to internal rotation and force field of 2, 2, 2-trifluoroacetamide as studied by gas electron diffraction and quantum chemical calculations, Journal of Molecular Structure 445(1-3) (1998) 229-242, doi:10.1016/S0022-2860(97)00427-4.

[82] S. Samdal, R. Seip, The molecular structure, conformation, potential to internal rotation and force field of 2, 2, 2-trichloroacetamide as studied by gas electron diffraction and quantum chemical calculations, Journal of Molecular Structure 413 (1997) 423-439, doi:10.1016/S0022-2860(97)00018-5.

[83] A.K. Rai, S. Kumar, A. Rai, Infrared, Raman spectra and DFT calculations of chlorine substituted anilines, Vibrational Spectroscopy 42(2) (2006) 397-402, doi:10.1016/j.vibspec.2006.05.033.

[84] F. Huang, Z. Rong, X. Shen, F. Huang, L. Du, Z. Li, Organic/inorganic hybrid bismaleimide resin with octa (aminophenyl) silsesquioxane, Polymer Engineering & Science 48(5) (2008) 1022-1028, doi:10.1002/pen.21046.

[85] S. Salimi, Experimental characterization and modelling of OAPS as a precursor for polyOAPS-imide membranes, LEPMI-GUIDE, University of Savoie Mont Blanc, France, 2022, p. 158.

[86] P.S.G. Krishnan, C. He, Octa (maleimido phenyl) silsesquioxane copolymers, Journal of Polymer Science Part A: Polymer Chemistry 43(12) (2005) 2483-2494, doi:10.1002/pola.20720.

[87] J. Zhang, R.W. Xu, D.S. Yu, A novel and facile method for the synthesis of octa (aminophenyl) silsesquioxane and its nanocomposites with bismaleimide‐diamine resin, Journal of Applied Polymer Science 103(2) (2007) 1004-1010, doi:10.1002/app.25290.

[88] M. Balci, Basic $^{1}$H-and $^{13}$C-NMR spectroscopy, Elsevier2005.

[89] J. Li, J.-K. Liu, W.-X. Wang, GIAO $^{13}$C NMR Calculation with Sorted Training Sets Improves Accuracy and Reliability for Structural Assignation, The Journal of Organic Chemistry 85(17) (2020) 11350-11358, doi:10.1021/acs.joc.0c01451.

[90] G. Barone, L. Gomez‐Paloma, D. Duca, A. Silvestri, R. Riccio, G. Bifulco, Structure validation of natural products by quantum‐mechanical GIAO calculations of $^{13}$C NMR chemical shifts, Chemistry‐A European Journal 8(14) (2002) 3233-3239, doi: 10.1002/1521-3765(20020715)8:14<3233::AID-CHEM3233>3.0.CO;2-0.

[91] G. Barone, D. Duca, A. Silvestri, L. Gomez‐Paloma, R. Riccio, G. Bifulco, Determination of the relative stereochemistry of flexible organic compounds by *ab initio* methods: conformational analysis and Boltzmann‐averaged GIAO $^{13}$C NMR chemical shifts, Chemistry‐A European Journal 8(14) (2002) 3240-3245, doi:10.1002/1521-3765(20020715)8:14<3240::AID-CHEM3240>3.0.CO;2-G.

[92] S.G. Smith, J.M. Goodman, Assigning stereochemistry to single diastereoisomers by GIAO NMR calculation: The DP4 probability, Journal of the American Chemical Society 132(37) (2010) 12946-12959, doi:10.1021/ja105035r.

[93] A.G. Kutateladze, D.S. Reddy, High-throughput in silico structure validation and revision of halogenated natural products is enabled by parametric corrections to DFT-computed $^{13}$C NMR chemical shifts and spin–spin coupling constants, The Journal of Organic Chemistry 82(7) (2017) 3368-3381, doi:10.1021/acs.joc.7b00188.

[94] G. Bifulco, P. Dambruoso, L. Gomez-Paloma, R. Riccio, Determination of relative configuration in organic compounds by NMR spectroscopy and computational methods, Chemical Reviews 107(9) (2007) 3744-3779, doi:10.1021/cr030733c.

[95] M.W. Lodewyk, M.R. Siebert, D.J. Tantillo, Computational prediction of $^{1}$H and $^{13}$C chemical shifts: a useful tool for natural product, mechanistic, and synthetic organic chemistry, Chemical Reviews 112(3) (2012) 1839-1862, doi:10.1021/cr200106v.

[96] E.D. Shepherd, B.S. Dyson, W.E. Hak, Q.N.N. Nguyen, M. Lee, M.J. Kim, T.-i. Sohn, D. Kim, J.W. Burton, R.S. Paton, Structure determination of a chloroenyne from Laurencia majuscula using computational methods and total synthesis, The Journal of Organic Chemistry 84(9) (2019) 4971-4991, doi:10.1021/acs.joc.8b02975.

[97] A. Wu, Y. Zhang, X. Xu, Y. Yan, Systematic studies on the computation of nuclear magnetic resonance shielding constants and chemical shifts: The density functional models, Journal of Computational Chemistry 28(15) (2007) 2431-2442, doi:10.1002/jcc.20641.

[98] K.K. Baldridge, J.S. Siegel, Correlation of empirical δ (TMS) and absolute NMR chemical shifts predicted by *ab initio* computations, The Journal of Physical Chemistry A 103(20) (1999) 4038-4042, doi:10.1021/jp990523x.

[99] D.B. Chesnut, On the calculation of hydrogen NMR chemical shielding, Chemical Physics 214(1) (1997) 73-79, doi:10.1016/S0301-0104(96)00296-0.

[100] K. Bahgat, S. Fraihat, Normal coordinate analysis, molecular structure, vibrational, electronic spectra and NMR investigation of 4-Amino-3-phenyl-$^{1}$H-1, 2, 4-triazole-5 (4H)-thione by *ab initio* HF and DFT method, Spectrochimica Acta Part A: Molecular and Biomolecular Spectroscopy 135 (2015) 1145-1155, doi:10.1016/j.saa.2014.05.081.

[101] H.C. Da Silva, W.B. De Almeida, Theoretical calculations of $^{1}$H NMR chemical shifts for nitrogenated compounds in chloroform solution, Chemical Physics 528 (2020) 110479, doi:10.1016/j.chemphys.2019.110479.

[102] C. Benzi, O. Crescenzi, M. Pavone, V. Barone, Reliable NMR chemical shifts for molecules in solution by methods rooted in density functional theory, Magnetic Resonance in Chemistry 42(S1) (2004) S57-S67, doi:10.1002/mrc.1447.

[103] Y. Zhang, A. Wu, X. Xu, Y. Yan, Geometric dependence of the B3LYP-predicted magnetic shieldings and chemical shifts, The Journal of Physical Chemistry A 111(38) (2007) 9431-9437, doi:10.1021/jp0740503.